

University of Central Florida

**STARS**

---

Electronic Theses and Dissertations, 2020-

---

2021

## On the Information Content in Unresolved Imaging

Zhean Shen

*University of Central Florida*



Part of the [Optics Commons](#)

Find similar works at: <https://stars.library.ucf.edu/etd2020>

University of Central Florida Libraries <http://library.ucf.edu>

This Doctoral Dissertation (Open Access) is brought to you for free and open access by STARS. It has been accepted for inclusion in Electronic Theses and Dissertations, 2020- by an authorized administrator of STARS. For more information, please contact [STARS@ucf.edu](mailto:STARS@ucf.edu).

---

### STARS Citation

Shen, Zhean, "On the Information Content in Unresolved Imaging" (2021). *Electronic Theses and Dissertations, 2020-*. 1346.

<https://stars.library.ucf.edu/etd2020/1346>

# ON THE INFORMATION CONTENT IN UNRESOLVED IMAGING

by

ZHEAN SHEN

B.E. Shanghai Jiaotong University, 2013  
M.S. Washington University in St. Louis, 2015

A dissertation submitted in partial fulfillment of the requirements  
for the degree of Doctor of Philosophy  
in the Department of Optics  
in the College of Optics and Photonics, CREOL  
at the University of Central Florida  
Orlando, Florida

Fall Term  
2021

Major Professor: Aristide Dogariu

© 2021 Zhean Shen

## ABSTRACT

Imaging is almost synonymous with optics. Imaging is the process of using light to form a tangible or visible representation, an imitation (*imitari*) of a material property. There are many situations, however, where one can only aspire to ‘sense making’ rather than forming an image *per se*. In other words, objects cannot be directly resolved by conventional intensity-based imaging, a situation commonly referred to as ‘unresolved imaging’. However, there is still information retained in other properties of light, which can be exposed by other means. In this thesis I will discuss two typical situations: subwavelength and multiple scattering, which are very different in terms of the spatial extent of light-matter interaction.

In the subwavelength regime, information can be encoded through both inelastic and elastic interaction processes. When the latter is the preferred approach, observables such as optical phase are determined by the properties of evanescent waves while the measurements are usually conducted in the far-field. I will describe a novel energetic interpretation of the light-matter interaction in this regime, which provides an accurate estimation of the interaction volume of a single scattering event and of the small phase delay it introduces. I will also show how this minute phase occurring in subwavelength scattering can be quantitatively measured with optimal sensitivity by a polarization-encoded common path system and how it enables subwavelength sizing in a label-free fashion.

At the other extreme, evaluating the information transfer in multiple scattering regimes is usually constrained by the computational complexity of the problem. I will describe two forward modeling approaches that alleviate these limitations in non-line-of-sight sensing geometries and

in coherent illumination methods for imaging through obscurants. These simplifying descriptions also reveal the fundamental limits for information transfer in these two scenarios.

## ACKNOWLEDGMENTS

I wish to acknowledge my advisor, Prof. Aristide Dogariu, for his support, guidance, and above all, his friendship, which has made this PhD an unforgettable journey. It is my pleasure and honor to work with him.

The Random Group is a place of inspiring discussions and interactions. Thanks to all of the current and former members for their invaluable support.

I wish to acknowledge my committee members, Prof. Pieter G. Kik, Prof. Kyu Young Han and Prof. Alexandru C. Tamasan, for their support and priceless suggestions.

I am grateful to Prof. Pieter G. Kik, Prof. Eric W. Van Stryland, Prof. Martin C. Richardson and Prof. Ayman Abouraddy for their excellent teaching.

I especially appreciate the companionship of Yuge Huang and inspirations from Ryozo Tsujimoto during the pandemic.

# TABLE OF CONTENTS

LIST OF FIGURES .....	viii
LIST OF TABLES .....	ix
CHAPTER ONE: INTRODUCTION .....	1
CHAPTER TWO: SENSING AT SUBWAVELENGTH SCALES .....	4
2.1 Meaning of Phase in Subwavelength Elastic Scattering .....	7
2.1.1 Group Delay .....	8
2.1.2 Dwell Time .....	11
2.1.3 Interaction Volume .....	14
2.1.4 Role of Evanescent Wave .....	18
2.2 Polarization-encoded Field Measurements .....	20
2.2.1 Field Measurement with Optimal Sensitivity .....	20
2.2.2 Subwavelength Sizing .....	26
2.2.3 Comparison between Imaging Modalities .....	28
CHAPTER THREE: SENSING IN MULTIPLE SCATTERING REGIMES .....	31
3.1 Monte Carlo Simulation of Spatial Coherence Propagation through Random Media .....	33
3.1.1 Wigner Monte Carlo Method .....	37
3.1.2 Numerical Simulation .....	39
3.1.3 Non-Line-of-Sight Imaging .....	45
3.1.4 Spatial Coherence after Surface and Volume Scattering .....	48
3.2 Vector Wave Simulation of Active Imaging through Random Media .....	55
3.2.1 Statistical Equivalence .....	55
3.2.2 Vector Wave Solution .....	61
3.2.3 Computational Capabilities .....	67
CHAPTER FOUR: CONCLUSION .....	69
LIST OF PUBLICATIONS .....	72

LIST OF REFERENCES ..... 73

## LIST OF FIGURES

Figure 1: Unresolved imaging.....	1
Figure 2: Imaging in multiple scattering regimes. ....	3
Figure 3: Geometric delay $\Delta g$ and phase delay $\Delta\phi$ . ....	9
Figure 4: Total field as the summation of incident field and scattered field.....	10
Figure 5: Interaction volume $V$ defining the dwell time $\tau w$ . ....	13
Figure 6: Dwell time $\tau w$ as a function of size of the interaction volume. ....	14
Figure 7: Comparison between $\Delta\phi$ and $\Delta w$ . ....	15
Figure 8: Scattering cross-section and interaction volume. ....	17
Figure 9: Deviations from independent scattering approximation (ISA).....	18
Figure 10: Polarization-encoded microscope.....	21
Figure 11: Measured intensities for phase-shifting method.....	25
Figure 12: Results of full reconstruction of the scattered fields .....	26
Figure 13: Relationship between the phase $\phi$ and the diameter $a$ of subwavelength particles. ....	28
Figure 14: Traditional Monte Carlo simulation of light propagation in scattering media. ....	35
Figure 15: The geometry of spatial coherence propagation.....	39
Figure 16: Comparison between Mie (blue solid line) and Henyey-Greenstein (red dashed line) scattering phase functions.....	41
Figure 17: Normalized SCF at the output of scattering media containing nearly forward scattering particles for different optical densities (OD). ....	42
Figure 18: Normalized SCF for the reflected light. ....	44
Figure 19: Different non-line-of-sight sensing conditions.....	46
Figure 20: Schematic representation of the field reflected from a diffusive wall and its SCF assessed for in-plane $s \parallel$ and out-of-plane $s \perp$ shears. ....	48
Figure 21: Spatial coherence and wall interpreted by Wigner Monte Carlo method.....	49
Figure 22: Distribution of generalized radiance for volume scattering. ....	50
Figure 23: Anisotropic transfer of spatial coherence. ....	51
Figure 24: Monte Carlo simulation for energy ratio between surface scattering and volume scattering....	52
Figure 25: Spatial coherence function measured for different field of view. ....	53
Figure 26: “Glitter path” effect in reflection from random media. ....	55
Figure 27: Simplified description of active imaging through a random medium comprising. ....	57
Figure 28: Distribution of random field at the aperture plane. ....	64
Figure 29: Measurements corresponding to one realization of the random medium.....	66

## LIST OF TABLES

Table 1: The full width at half maximum (FWHM) of the spatial coherence function estimated from different approaches.....	43
---	----

## CHAPTER ONE: INTRODUCTION

Optical imaging is one of the most ancient branches in optics [1], and the philosophy behind can be summarized as transferring information from one point to another, as shown in Figure 1(a). In most cases, optical imaging system can be simplified as a linear, shift-invariant system, where the acquired image is the convolution between object and point spread function (PSF) [1]. As shown in Figure 1(a), convolution with PSF induces unavoidable information loss like blurring. Blurring can be tolerable or devastating, depending on the scenario. For example, we suppose that objects are two points separated by a certain distance, as shown in Figure 1(b). If the distance is larger than the width of PSF, it is defined as fully resolved; if the distance is comparable to the width of PSF, it is defined as just resolved; if the distance is smaller than the width of PSF, it is defined as unresolved. In the following, we will focus on two unresolved scenarios: subwavelength and multiple scattering.

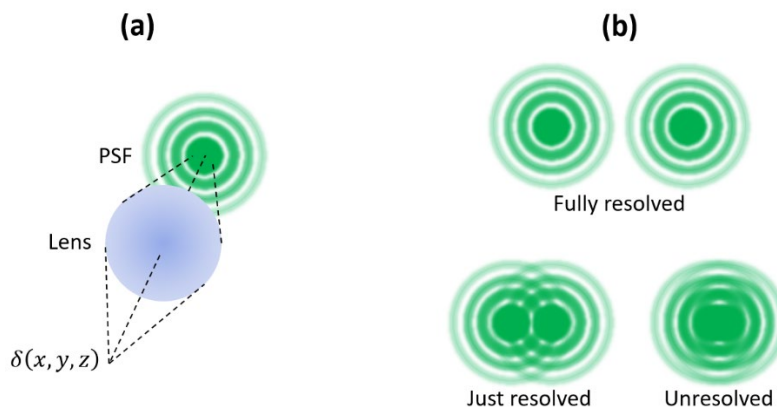


Figure 1: Unresolved imaging.

(a) Imaging system. (b) Three scenarios: fully resolved, just resolved and unresolved.

Adapted from Wikipedia:

[https://en.wikipedia.org/wiki/Angular\\_resolution](https://en.wikipedia.org/wiki/Angular_resolution)

Optical imaging is an important tool in biomedical research, since many common sense in biology are kept updated through these delicate instruments [2]. Optical imaging is especially useful in unveiling the biological structures under microscopic scale, like cell [3]. Cells function as the basic blocks of most creatures and they can copy themselves in most cases, which is called mitosis [4]. It is well known that centrosome plays an important role during mitosis; however, the mechanism behind still requires more exploration. The size of centrosome is roughly 300 nm, which is smaller than the wavelength of visible light. Of course, X ray can be used to recover its structure [5]; however, phototoxicity limits illuminating X ray on cell in vivo. Therefore, it is ideal to use visible light to recover spatial information smaller than 300 nm, which is exactly subwavelength. There are already some well-established methods, like super-resolution [3]. However, super-resolution requires labeling samples with fluorophores, which has several disadvantages like photon-bleaching and limited photon flux [6]. In Chapter 2, subwavelength information is recovered by label-free methods like phase. I will discuss the meaning of phase in subwavelength scattering using an energetic perspective and introduce one efficient method to quantitatively measure this tiny phase by polarization encoding [7].

Optical imaging is also important in remote sensing. For scenarios like self-driving car, environment-induced scattering is unavoidable because of fog and rain [8]. As shown in Figure 2(b), these scenarios are like adding a diffuser into a perfect optical imaging system, where the corresponding PSF will be largely extended and noisy. Therefore, multiple scattering is another type of ‘unresolved imaging’, which will be the theme in Chapter 3. Due to the complexity of the problem, it is very meaningful to build up simplified forward models which only require computing resources afforded by commercial machines. In Chapter 3, I will focus on two specific

scattering scenarios: non-line-of-sight imaging [9, 10] and imaging through obscurants. For non-line-of-sight imaging, I will discuss how the information of object is preserved in spatial coherence even after scattering. For imaging through obscurants, I will introduce one efficient method to modeling vectorial wave properties of macroscopic scattering [11].

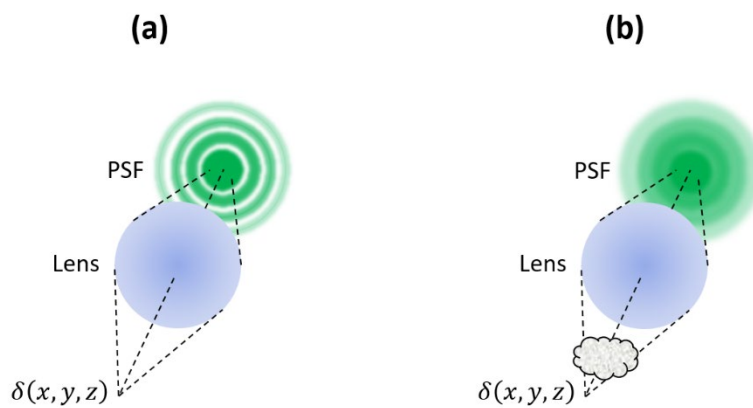


Figure 2: Imaging in multiple scattering regimes.

(a) Optical imaging without multiple scattering. (b) Optical imaging influenced by multiple scattering.

## CHAPTER TWO: SENSING AT SUBWAVELENGTH SCALES

In this chapter, subwavelength information is recovered through phase, which is label-free. Label-free methods are quite universal, thus enabling wide applications in biomedical research. The first part in this chapter is about the meaning of phase in subwavelength scattering, and the second part is about quantitative measurement of this tiny phase.

Phase is a relative measure of two stages of an oscillation. At a given frequency, the phase defines the velocity with which the energy transfers while surfaces of equal phase constitute the wavefront of a propagating wave. Experimentally, the phase is obtained as the dimensionless delay between two different wavefront measurements [12, 13].

Even though it is usually determined indirectly, phase is an important wave parameter describing the propagation and, most importantly, the consequences of the interaction between waves and matter. In practice, this information is typically recovered from intensity measurements performed on the superposition (interference) of a reference and an object beam that has interacted with the object.

A plane wave impinging on an infinite slab of thickness  $a$  is a one-dimensional scattering problem that recorded leads to an acquired phase measured as a “geometric delay”  $\Delta_g = a(n_s - n_b)/c$  where  $c$  is the velocity of light in vacuum while  $n_s$  and  $n_b$  are the effective refractive indices of the object and its environment, respectively [14].

Real objects have finite extent and perturb the field everywhere. The effect of three-dimensional scattering is usually felt over domains larger than the physical volume occupied by the object. The transformation of an incident plane wave  $\mathbf{E}_i$  onto a superposition of multiple plane

waves is described by an amplitude scattering matrix,  $\mathbf{E}_s(r, \theta, \varphi) = f(r)\overline{\mathbf{S}}(\theta, \varphi)\mathbf{E}_i(\varphi)$ , which describes the particular weight and the specific delay of each output channel [15]. After the influence  $f(r)$  of propagation is eliminated, these delays are customarily evaluated in the far-field in a manner similar to the one-dimensional scattering mentioned before. Thus, in steady-state situations, the scattering of monochromatic fields can be characterized by “geometric delays” irrespective of the dimensionality of the interaction problem.

In the following sections, the delay will be compared between two canonical phenomena: retardation by an infinite slab and scattering by a finite particle. Interestingly, huge differences exist in both quantities and mechanisms of these two phenomena. We will find that evanescent wave plays a key role in the phase of subwavelength scattering. This enables a better understanding of phase and provides more clues for recovering subwavelength information.

The phase and amplitude of optical fields can be measured in different ways. For instance, one can use direct intensity measurements across an optical wavefront to directly determine the amplitude and then use phase retrieval algorithms that rely on different levels of a priori information [16]. When information about the optical situation is not available, one can use interferometric methods where the intensity measurements are performed on the superposition of two wavefronts, the object field to be characterized and a controlled reference field.

The field superposition can be realized in many ways. The most straightforward approach is to bring the fields into the region of interference via physically distinct paths. However, because the inherent distortions along the paths can be different, the stability of this scheme is prone to environmental perturbations. This issue can be mitigated by forcing the two fields to travel along the same physical path in a so-called common-path design [17].

A common-path interferometer is in fact generated in any scattering event where the incident field combines naturally with the field scattered by a distant object. Let us consider the net field generated as a result of the interaction between a plane-wave incident field and an object. When this superposition field is analyzed in its directional space (Fourier domain), the zero-frequency (DC) component represents the spatial average across the net field, which can also be regarded as a ‘virtual’ reference for the scattered field characterized by higher spatial frequencies. Of course, these two field components mix during propagation through the same optical path but, importantly, they are physically separated in the Fourier domain. Thus, in this plane, both the phase and the amplitude of the ‘virtual’ reference can be modified such that the desired information about the scattered field can be extracted from intensity measurements performed in another plane, e.g. in the imaging plane. This interpretation goes back to the original Zernike’s designs and is the essence of several microscopy techniques [18].

Nevertheless, this common-path scheme has several major shortcomings. First, the achievable fidelity or spatial resolution is limited because the ‘virtual’ reference field cannot be a pure DC signal. The finite extent of optical beams and the limited size of optical components force the ‘virtual’ reference to extend over a certain range of small spatial frequencies, which makes the scattered field to be practically band-limited.

The second limitation relates to the interferometric visibility. Experimentally, the desired information is determined from relative intensity measurements, i.e. from interferograms visibilities, which vary when adjusting the phase of the reference. Of course, the maximum visibility contrast can only be achieved when two fields have the same amplitude. This is hardly

the case for the extremely inefficient subwavelength scattering where the strength of the scattered field is much weaker than the reference.

Finally, it is the notion of phase itself. Since the energy transport in subwavelength scattering is largely influenced by evanescent fields, the scattered wave is released out almost instantaneously. As a result, the measurable phase is significantly smaller than the so-called ‘geometric delay’, which is usually derived in terms of phase-velocity. This specific feature of subwavelength scattering imposes a necessarily higher resolution for the phase measurement [19].

The experimental characteristics discussed above are major impediments when measuring the optical phase associated with subwavelength objects. To alleviate these limitations, an optimal measurement of the scattered field should be performed in a common-path setting and it should provide control over both the phase and amplitude of the reference field. In the following sections, we will show how this can be achieved by controlling the polarization states of the two fields while using a conventional 4f optical system.

### 2.1 Meaning of Phase in Subwavelength Elastic Scattering

We have seen that phase is interpreted as a dimensionless delay and is one of the major consequences of light-matter interaction. However, a simplistic geometric interpretation of the measured phase is insufficient when the scattering center is smaller than the wavelength (subwavelength). In this section, energetic arguments have been used to describe appropriately the phase measured far away from subwavelength objects. Evanescent field is found to have significant contributions in coupling and releasing of energy during subwavelength scattering and

is the main cause of the extremely small phase. In addition, the comparison between delays in near and far field enables estimating the duration and the effective volume of an elastic scattering event.

### 2.1.1 Group Delay

In the case of non-stationary scattering phenomena involving more complex waves with broader bandwidth, one can invoke, in the far field, a stationary-phase approximation and define a “phase delay”  $\Delta_\phi$  as the derivative of the phase accumulated in each spectral channel [20, 21, 22]. The differences between  $\Delta_\phi$  and  $\Delta_g$  will therefore depend on the way a far-field measurement is conducted. This is illustrated in Figure 3 where the time delay due to scattering on a polystyrene sphere is compared to the delay produced by a polystyrene slab with the same thickness as the particle’s diameter. The phase delay is calculated by Mie scattering for spheres with different diameters placed in air and continuously illuminated by a laser with central wavelength 532 nm and a coherence time of 20 ns.

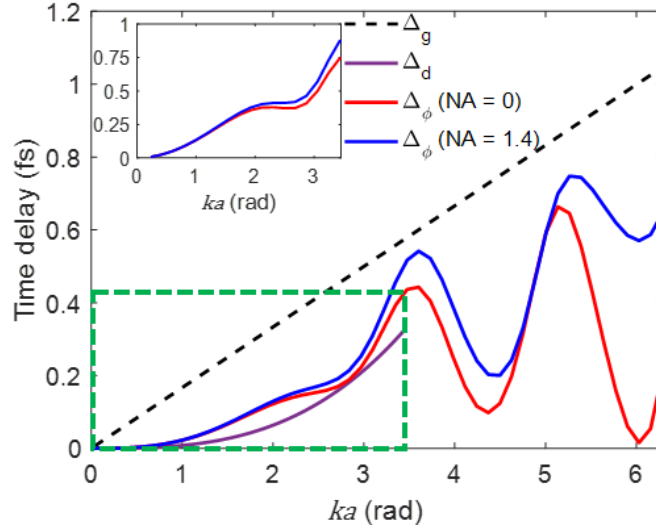


Figure 3: Geometric delay  $\Delta_g$  and phase delay  $\Delta_\phi$ .

Geometric delay  $\Delta_g$  and phase delay  $\Delta_\phi$  as a function of size  $a$  of subwavelength particles ( $k = 2\pi/\lambda$  is the vacuum wavenumber). Also shown is time delay  $\Delta_d$  corresponding to dipolar scattering (see text). The inset shows the ratio  $\Delta_\phi/\Delta_g$  evaluated over the range indicated by the green dashed line.

As seen, while  $\Delta_g$  increases linearly with particle size, the  $\Delta_\phi$  dependence on  $a$  is more complicated. After a certain threshold, the phase delay actually fluctuates, which precludes a unique determination of the particle size from measurements of  $\Delta_\phi$ . Notably, the value of the determined  $\Delta_\phi$  significantly depends on the numerical aperture (NA) of the detection system but this influence diminishes for smaller particles.

In fact, for smaller particles,  $\Delta_\phi$  becomes much lower than  $\Delta_g$  as evident in the inset of Figure 3. In other words, the mechanism of subwavelength scattering cannot be described by a geometric delay  $\Delta_g$  and interpreted as a simple retardation.

A simpler interpretation can be advanced when the particle is much smaller than the wavelength; the scattering field resembles the radiation emitted by a dipole with an electric

polarizability that also accounts for a radiative reaction [23, 24]. It can be shown that this dipolar scattering introduces a temporal delay  $\Delta_d = \frac{\pi^2 a^3 (n_s/n_b)^2 - 1}{3c\lambda^2 (n_s/n_b)^2 + 2}$ . As evident in Figure 3, the “dipolar delay”  $\Delta_d$  matches  $\Delta_\phi$  in the small particle limit when  $a \ll \lambda$ .

The phase or time delays surveyed so far were practically evaluated as far-field consequences of a scattering event as illustrated generically in Figure 4. This far-field description does not provide insights into the process itself. In particular, far-field measurements do not explain how the field was modified by the presence of the object and what the duration of this transformation was. For this, one must appeal to a near-field description of the wave-matter interaction. How the emerging wave can be regarded as the superposition of the incident wave and all the fields radiated by the oscillating atoms that constitute the particle is well framed within the Ewald-Oseen theorem [25].

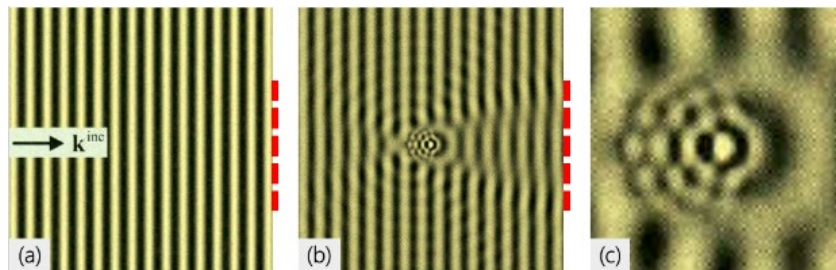


Figure 4: Total field as the summation of incident field and scattered field.

A scattering event describes the transformation between initial (a) and final (b) field configurations. The outcome of scattering is usually quantified after the wave has propagated in the far-field, as indicated by the red dotted lines. Explaining how this transformation occurred requires a near-field examination (c).

### 2.1.2 Dwell Time

An intuitive description of the duration of an elastic scattering event can be based on energetic arguments. When placed in an electromagnetic field, material objects store electric and magnetic energy before releasing it after a “dwell time”  $\tau_w$ . This time is then evaluated as the ratio between the stored energy and the outgoing flux. The problem is typical for any quantity that transits through a finite volume of space, which is subject to incoming and outgoing fluxes [26, 27]. It is an open system description of the scattering process, which allows evaluating the difference (delay) between the dwell times corresponding to different materials filling up the same volume of space.

The dwell time evaluation requires first to delineate an interaction volume  $V$  where the “stored energy” is to be evaluated and then assess the outward energy flux through the surface  $A$  that bounds this volume. The total outgoing flux can be calculated using the energy flux density (irradiance)  $\mathcal{S}_{out}(\mathbf{r})$  defined such  $\mathcal{S}(\mathbf{r}) \cdot \mathbf{n}(\mathbf{r}) > 0$  with respect to the local outward normal to the surface  $\mathbf{n}(\mathbf{r})$ . The dwell time is defined as

$$\tau_w = \frac{\iiint_{(V)} \langle u(\mathbf{r}) \rangle d\mathbf{r}^3}{\iint_{(A)} \mathcal{S}_{out}(\mathbf{r}) \cdot \mathbf{n}(\mathbf{r}) d\mathbf{r}^2}, \quad (1)$$

where  $\langle u(\mathbf{r}) \rangle$  represents the density of electromagnetic energy within the interaction volume. Integrating  $\langle u(\mathbf{r}) \rangle$  over the physical volume of large objects provides a good estimate.

For subwavelength size particles, however, a significant portion of the interaction energy resides outside the physical boundary and it is stored as evanescent fields. Even though the evanescent fields do not propagate they can store and release energy, which is a process that takes additional time [22]. In fact, the evanescent fields act as an additional shell-like ‘energy capacitor’,

which is an inseparable part of energy transfer during the scattering event. Thus, the effective interaction volume  $V$  is practically larger than the particle's physical volume.

We will now outline the practical procedure for evaluating  $\tau_w$ . It is customary to interpret the final field illustrated in Figure 4(b) as a superposition of an initial field (plane wave for simplicity)  $\mathbf{E}_i, \mathbf{H}_i$  that exists in the absence of the scatterer and a scattered field  $\mathbf{E}_s(\mathbf{r}), \mathbf{H}_s(\mathbf{r})$ , which is merely a mathematical convenience [28]. In these conditions, the local irradiance  $\mathbf{S}(\mathbf{r})$  is the summation of three different terms:  $\mathbf{S}_i = \frac{1}{2} \text{Re}\{\mathbf{E}_i \times \mathbf{H}_i^*\}$ ,  $\mathbf{S}_s(\mathbf{r}) = \frac{1}{2} \text{Re}\{\mathbf{E}_s(\mathbf{r}) \times \mathbf{H}_s^*(\mathbf{r})\}$  and a contribution  $\mathbf{S}_{ext}(\mathbf{r}) = \frac{1}{2} \text{Re}\{\mathbf{E}_i \times \mathbf{H}_s^*(\mathbf{r}) + \mathbf{E}_s(\mathbf{r}) \times \mathbf{H}_i^*\}$  from the interference of the two fields.

It follows that the net energy flux across the surface  $A$  of the interaction volume,  $\Phi = \iint_{(A)} \mathbf{S}(\mathbf{r}) \cdot \mathbf{n}(\mathbf{r}) d\mathbf{r}^2$ , comprises three terms corresponding to the three different flux densities. The net flux contributions can also be classified in terms of inward  $\Phi^{(+)}$  and outward  $\Phi^{(-)}$  components. For instance, the net flux corresponding to a plane wave incident is zero:  $\Phi_i^{(+)} + \Phi_i^{(-)} = 0$ . Since  $\mathbf{S}_s(\mathbf{r})$  always points away from the surface,  $\Phi_s^{(-)} = \iint_{(A)} \mathbf{S}_s(\mathbf{r}) \cdot \mathbf{n}(\mathbf{r}) d\mathbf{r}^2$  is always an outward flux. This means that the flux balance becomes  $\Phi = \Phi_i^{(+)} + \Phi_{ext}^{(+)} + \Phi_i^{(-)} + \Phi_{ext}^{(-)} + \Phi_s^{(-)}$ . Using the usual definition of the so-called scattering cross-section,  $\sigma_{sc} = |\mathbf{S}_i|^{-1} \iint_{(A)} \mathbf{S}_s(\mathbf{r}) \cdot \mathbf{n}(\mathbf{r}) d\mathbf{r}^2$ ,  $\Phi_s^{(-)}$  can also be written as  $\sigma_{sc} |\mathbf{S}_i|$  [15].

The circumstances of subwavelength, elastic scattering permit further simplifications. In this case, the scattered field is much weaker than the initial field even at the surface of the scatterer, which is the reason for the fast-decaying scattering cross section when  $a \ll \lambda$  [15]. Therefore,  $|\mathbf{S}_i| \gg |\mathbf{S}_{ext}(\mathbf{r})| \gg |\mathbf{S}_s(\mathbf{r})|$  and the outgoing flux  $\Phi^{(-)}$  is dominated by  $\Phi_i^{(-)}$ , which leads to

$$\tau_w \approx \frac{\iiint_V \langle u(\mathbf{r}) \rangle d\mathbf{r}^3}{\Phi_i^{(-)}}. \quad (2)$$

This also explains the unphysical divergence of estimated  $\tau_w$  if  $\Phi^{(-)}$  is approximated as  $\Phi_s^{(-)}$ , which is intuitive but severely underestimates the outgoing flux [29].

We will now outline a procedure for correct estimation of the outgoing flux. Let us consider a plane wave impinging on a cubic domain of size  $l$  surrounding a small scattering particle of size  $a < l$  as illustrated in Figure 5. In these conditions, the outgoing flux is simply  $\Phi^{(-)} = l^2 |\mathcal{S}_i|$  and the dwell time can be evaluated from Eq. (2) to be

$$\tau_w \approx \frac{\iiint_{cube} \langle u(\mathbf{r}) \rangle d\mathbf{r}^3}{l^2 |\mathcal{S}_i|}. \quad (3)$$

In general, for particles of arbitrary shapes and sizes, the energy density and, consequently, the dwell time must be calculated numerically [15, 30, 31]. We note that for spherical particles the interior energy density can be evaluated analytically [32] and that, in many situations of practical interest, a spherical shape approximation for subwavelength particles may be sufficient [33].

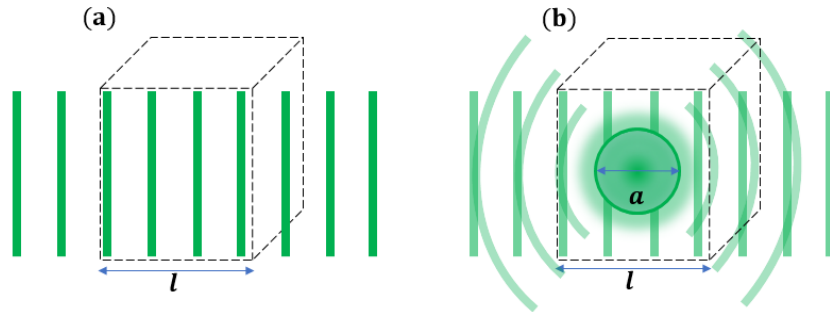


Figure 5: Interaction volume  $V$  defining the dwell time  $\tau_w$ .

(a) Free space propagation. (b) Scattering by a small particle.

### 2.1.3 Interaction Volume

Of course, the estimation of  $\tau_w$  is affected by the size  $l$  of the interaction volume. This is illustrated schematically in Figure 6, where  $\tau_w$  is evaluated for increasing sizes of the interaction volume. For larger  $l$ , the estimated dwell time approaches the time necessary for a plane wave to freely propagate over the same distance. In this case, the presence of the particle has a little effect on the overall energy and, consequently, there is just a small difference between the duration of the process with and without the scatterer.

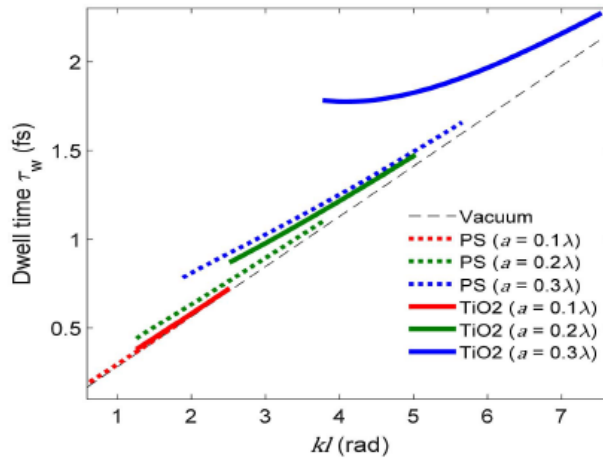


Figure 6: Dwell time  $\tau_w$  as a function of size of the interaction volume.

Dwell time  $\tau_w$  as a function of size of the interaction volume for spherical particles of polystyrene (PS) and TiO2 in air and with sizes as indicated.

This energetic interpretation provides a quantitative estimation of the event duration. Nevertheless, the practically relevant quantity is actually the delay introduced by the scattering event, i.e. the difference between the duration (dwell time) of the scattering process and the

duration of the free space propagation through the same volume of space. In other words, the practically relevant quantity is the time delay  $\Delta_w = \tau_w - \frac{l}{c}n_b$ .

It is instructive to compare the energetically evaluated time delay  $\Delta_w$  with the other delays discussed previously as illustrated in Figure 7 for microspheres of polystyrene and TiO<sub>2</sub>. First, one can see that for small particle sizes  $\Delta_g$  is the largest delay as expected. Second, for particle diameters smaller than approximately 0.3 the differences between  $\Delta_w$  and  $\Delta_\phi$  are rather insignificant, and are mainly due to the size of interaction volume over which  $\Delta_w$  is estimated. For reference, we have also plotted the corresponding ratio between  $\Delta_\phi$  evaluated on-axis and  $\Delta_g$ .

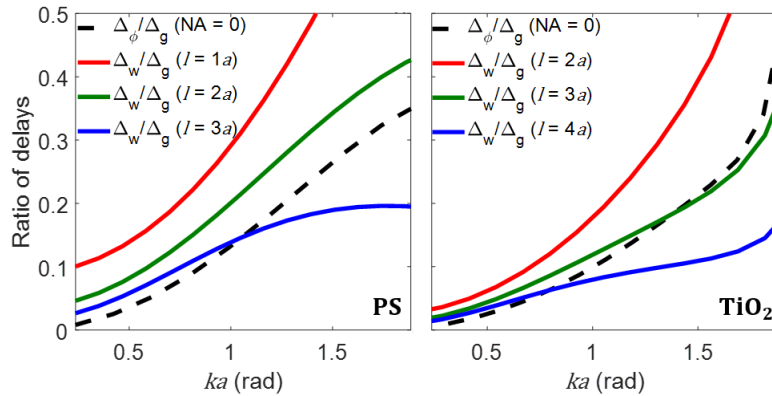


Figure 7: Comparison between  $\Delta_\phi$  and  $\Delta_w$ .

A rough comparison between  $\Delta_\phi$  and  $\Delta_w$  is conducted when the size of the interaction volume  $l$  is changed for PS and TiO<sub>2</sub> particles of different sizes  $ka$ .

The differences between  $\Delta_w$  and  $\Delta_\phi$  originate in the near-field and, respectively, far-field descriptions of the scattering event. Of course, when measured far away, the consequences of the event should be the same irrespective of the particular description. The similarity between the

predictions of near-field and far-field estimates can be used as a criterion for identifying the effective interaction volume. The size  $l_{opt}$  for which  $\Delta_\phi$  is well approximated by  $\Delta_w$  defines practically the “optical volume” of that particular event as seen from the far-field. For instance, the optical size of a PS sphere in air is about two times its physical size, while for TiO<sub>2</sub> sphere its size is three times. One can conclude that this energy-based evaluation can estimate not only the duration but also the interaction volume of a subwavelength scattering event.

Traditionally, the amount of light “intercepted” by a particle is gauged by its scattering cross-section. The efficiency of a scattering event is then determined by comparing this cross-section to the geometrical area exposed to the incident field. For subwavelength particles, the scattering cross-section can be much smaller than the physical size and this comparison of planar properties is inadequate. In fact, as shown in Figure 8, the “optical volume”  $l_{opt}^3$  over which a subwavelength particle modifies appreciably the incident field is significantly larger than a simple estimation such as  $V \sim \sigma_{sc}^{3/2}$ . We emphasize that, although the particle interacts with light over a volume much larger than its physical size, only a very small portion of the incident flux is deflected from its original direction, which leads to a very small scattering efficiency of the order of  $\sigma_{sc}/a^2$ . In other words, the concept of radiation “interception” is insufficient to describe the three-dimensional “interaction” between light and subwavelength particles.

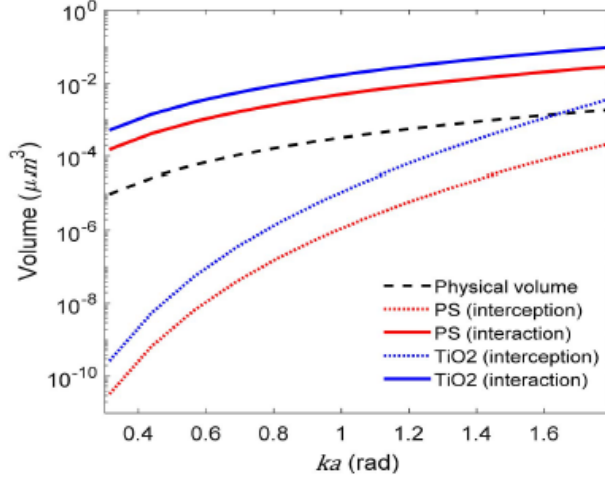


Figure 8: Scattering cross-section and interaction volume.

The volumes associated with the scattering event estimated based on the scattering cross-section  $\sigma_{sc}^{3/2}$  (planar interception) and evaluated based on the scattering dwell time  $l_{opt}^3$  (volumetric interaction). Also shown is the physical volume  $a^3$  of the subwavelength particle.

Such an estimate of the physical volume of interaction is particularly relevant in situations where light-matter interaction is described as heavy multiply scattering process. When the structural morphology of the medium forces the optical volumes to intersect, qualitatively different stages of light propagation are expected to occur [34, 35]. In this context, the size of the effective optical volume that we have introduced sets the higher limit for the so-called the independent scattering approximation (ISA) [36]. Figure 9 clearly demonstrates the capability of  $l_{opt}^3$  to anticipate the regimes where ISA-like models, or interception-based descriptions, are insufficient to describe the experiments. For several representative examples, we compare the experimental data from Refs [37, 38, 39] that indicate the ISA failure with our corresponding predictions based the volume of interactions evaluated using the procedure outlined before. As can be seen, in all cases, the departure from the ISA-like interpretations, or, in other words, “interception” based

models, correspond to volume fractions of scatterers for which the interaction volumes  $l_{opt}^3$  of neighboring particles start to intersect.

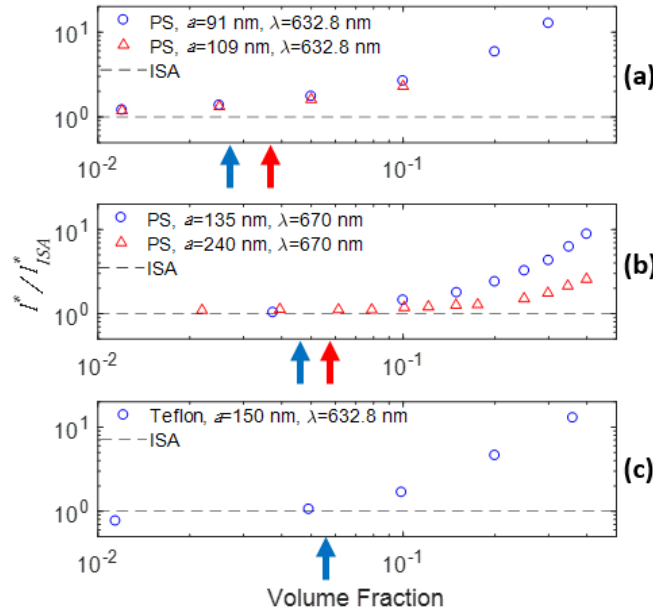


Figure 9: Deviations from independent scattering approximation (ISA).

Deviations of measured transport mean free path  $l^*$  from the values  $l^*_{ISA}$  estimated using ISA. Arrows indicate the threshold volume fractions for which the interaction volumes  $l_{opt}^3$  of neighboring particles will start to intersect. The experimental data are taken from different literature reports and correspond to (a) polystyrene (PS) particles illuminated by 632.8 nm [37], (b) PS particles illuminated by 670 nm [38], and (c) teflon particles illuminated by 632.8 nm [39].

#### 2.1.4 Role of Evanescent Wave

We will now summarize the conclusions of our communication. Any inverse problem relies on a forward model. When one attempts to recover the average size of subwavelength particles ( $ka < 2\pi$ ), significant errors are expected if the geometric delay time  $\Delta_g$  is used to model the results of a phase measurement. This is because of two main reasons. First, the scattering by a

subwavelength particle is not a simple retardation of propagating waves and, second, the effective volume of interaction is much larger than the physical size of the particle.

Retardation neglects the role of evanescent fields surrounding the particle. The evanescent fields constitute an additional, special path for storing and releasing energy, which is almost instantaneous for energy transportation. This is why the real-time delay in subwavelength elastic scattering can be much smaller than the intuitive estimation  $\Delta_g$  based on retardation of propagating waves. It also means that the existence and the specific characteristics of evanescent fields can affect the results of temporal measurements performed in the far field.

Subwavelength scattering is essentially a three-dimensional phenomenon. A subwavelength particle disturbs the incident field over scales much larger than its physical volume or any other estimate based on planar wave intercepts. This effectively larger volume of interaction defines a non-local boundary of interaction that is necessary to evaluate the energetic interaction and the consequent time delay. This non-local boundary is different from that in generalized Ewald–Oseen theorem, which is introduced as a gauge boundary for solving the electromagnetic field distribution [40, 41, 42, 43].

Neither the exact duration nor the effective interaction volume of a subwavelength scattering event can be directly measured in the far field. However, if the energetic time delay  $\Delta_w$  can be approximated by the measured phase delay  $\Delta_\phi$ , which is always the case for steady-state scattering, then an effective interaction volume can be estimated accurately. To eliminate any unphysical divergences [29], the procedure requires a complete treatment of the energy and fluxes that describe a subwavelength scattering event as we have shown here.

Finally, we should mention that, in principle, a similar treatment could be conducted for anisotropically structured materials. In such cases, the dwell times could vary along different directions, which is a topic beyond the scope of this paper.

Aside from providing a correct description of the phase measured in scattering by a subwavelength particle, our results afford new means for understanding the wave transport through media where scattering centers are in close proximity of each other and can be used to describe the wave propagation across different regimes of propagation as demonstrated here.

## 2.2 Polarization-encoded Field Measurements

In this section, polarization encoding is introduced, which enables measuring both phase and amplitude of optical scattered field with optimal sensitivity. The measured phase is further applied to estimate the size of subwavelength particle, thus converting the phase sensitivity to spatial resolution.

### 2.2.1 Field Measurement with Optimal Sensitivity

Let us consider a plane wave illuminating an object situated at plane (O) as shown in Figure 10. After scattering, the net field is mapped to a linearly polarized state oriented at  $\theta_1$  as indicated. In the back focal plane of the collecting lens F1, a home-made special polarizer (SP) creates the polarization encoding across the distribution of spatial frequencies. The special polarizer is fabricated by cutting and aligning a linear polarizing laminated film with a measured extinction ratio better than 120:1. Specifically, this special polarizer maps the reference and scattered fields onto orthogonal linearly polarized states. The orientation of these states determines the reference

system for our measurement. Note that ratio between the magnitudes of the reference and scattered fields can be arbitrarily and continuously modified by adjusting the angular orientation  $\theta_1$  within the extinction ratio limit.

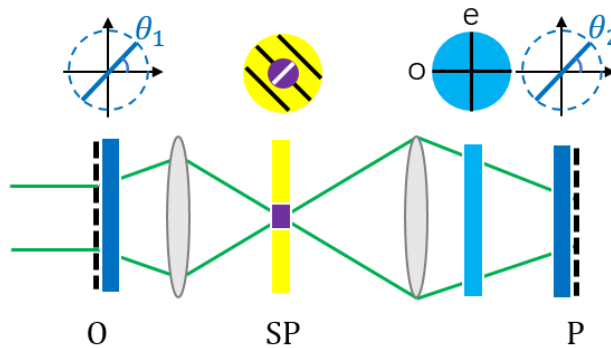


Figure 10: Polarization-encoded microscope.

A conventional 4f imaging system maps the object plane O into an image plane P via an intermediate Fourier plane where a special polarizer SP is located.

The special polarizer, two linear polarizers and a quarter-wave plate are used for the phase-to-polarization encoding and for measuring the scattered field across the plane O. The quarter-wave plate further converts the orthogonal polarizations into left and right circular states ( $L, R$ ). After the second Fourier lens, the two fields are again spatially overlapped in the conjugate (imaging) plane (P). Here, the interference between  $L, R$  is projected onto a common linearly polarized state  $\theta_2$  and, in this way, an additional phase delay is added between two fields. In the Poincaré sphere representation for the states of polarization, the magnitude of this phase delay is proportional to the area of spherical triangle  $LR\theta_2$  and represents the so-called geometric phase

[44]. The quality of polarization elements affect the polarization states  $L, R, \theta_2$  and influence the value of imposed geometric phase, which brings uncertainty to measurements.

For fixed alignments of the special polarizer encoder and the quarter wave plate, the intensity in the imaging plane depends solely on the orientations of  $\theta_1$  and  $\theta_2$  of the two polarizers.

At an arbitrary spatial location  $\mathbf{x}$  in the plane P, the intensity  $I(\mathbf{x}; \theta_1, \theta_2)$  varies as:

$$I(\mathbf{x}; \theta_1, \theta_2) = A_r^2(\mathbf{x}; \theta_1) \{1 + \gamma^2(\mathbf{x}; \theta_1) + 2\gamma(\mathbf{x}; \theta_1) \cos[\phi(\mathbf{x}) + 2\theta_2]\}, \quad (4)$$

where  $\gamma(\mathbf{x}; \theta_1) = A_s(\mathbf{x}; \theta_1)/A_r(\mathbf{x}; \theta_1)$  is the ratio between the amplitudes of scattered and reference fields and  $\phi(\mathbf{x})$  is the original phase between two fields.

As can be seen,  $A_r^2(\mathbf{x}; \theta_1)$  is readily obtained by adjusting  $\theta_1$  to cancel the scattered component  $A_s(\mathbf{x}; \theta_1) \rightarrow 0$  irrespective of the orientation of the second polarizer. Most importantly, an optimal visibility at each location  $\mathbf{x}$  can be attained by an independent adjustment of  $\theta_1$  such that  $\gamma(\mathbf{x}; \theta_1) \rightarrow 1$ . Moreover, for a fixed position  $\theta_1$  one can adjust  $\theta_2$  to generate the number of intensity values necessary to determine the desired phase  $\phi(\mathbf{x})$  by following any conventional phase-shifting method. For simplicity, in the following we will use a four-step method for phase extraction [45]. Having determined the amplitude of the reference field and the phase  $\phi(\mathbf{x})$ , the amplitude of the scattered field  $A_s(\mathbf{x}; \theta_1)$  can be easily determined from Eq. (4). Following this procedure, the complete field recovery requires five independent intensity measurements, one to determine the intensity of the reference field and four additional ones to recover the phase of scattered field.

Let us turn our attention to the measurement sensitivity. The amplitude and phase of the scattered field are retrieved from measured intensities, which fluctuate because of different reasons. Even though the environmental fluctuations are effectively cancelled in our common-path

configuration, the recorded intensities are still affected by the photon shot noise and other inherent instrumentation influences such as thermal noise, read noise, quantization error, etc. Normally, the signal-to-noise ratio (SNR) of a measurement can be improved by simply collecting more photons. However, for each frame, the maximum measurable intensity is limited by the pixel well capacity and, when the pixel well capacity is fully used, the photon shot noise is the dominant source of fluctuations. Recovering the phase requires multiple such intensity measurements and the phase uncertainty minimizes when the visibility of the interferogram approaches unity. This optimal condition can be reached in our procedure and, in this case, the phase uncertainty is simply inversely proportional with the pixel well capacity [46]. Therefore our method can make the best use of a given array detector.

We designed an experiment to test the sensitivity of this common-path design for optical field measurements. Subwavelength particles are chosen as the scattering units, since both the amplitude and the phase of the scattered field are small. The samples for subwavelength scattering are polystyrene particles of 46 nm diameter, which are randomly distributed and fixed in hydrogel (more than 90% water by weight). The fractional volume is low ( $2.6 \times 10^{-6}$ ), but during the mixing multiple particles may aggregate into larger clusters which are still subwavelength in size. Due to the viscosity of hydrogel, all subwavelength scatterers are suspended in a truly homogenous dielectric environment, thus avoiding the near-field coupling between particles and cover glass. In Figure 11 we show a typical region of the sample selected to include subwavelength clusters of different sizes. The intensity images corresponding to different clusters have similar extent as determined by the limited point spread function (PSF) of the imaging system. There are however

subtle differences in the intensity contrast around each of these scattering units (this is the signal exploited in the so-called iSCAT to estimate the volume of subwavelength particles) [47].

The measurement procedure is as follows. First, to measure  $A_r^2(\mathbf{x}; \theta_1)$  directly, the polarizer  $\theta_1$  is oriented at  $45^\circ$  such that it is parallel to the polarization state at the center of the special polarizer. In this position, the value of  $\gamma(\mathbf{x}; \theta_1)$  is minimized. Since  $A_r^2(\mathbf{x}; \theta_1)$  increases significantly when  $\theta_1$  approaches  $45^\circ$ , the camera exposure time should be controlled to avoid overexposure. An example of such image is shown in the bottom left panel of Figure 11.

Next, the orientation of  $\theta_1$  is set to assure the optimal visibility in the interference described by Eq. (4). Ideally, this should happen for  $\theta_1$  approaching  $-45^\circ$  as illustrated in bottom right panel of Figure 11 where we show the normalized interferograms for the particular region (a) with different orientations  $\theta_1$  of the first polarizer. Because in this proof-of-concept experiment the special polarizer had an extinction ratio limited to 120:1, the interferogram does not reach the ideal condition of zero intensity for  $\theta_2 = 90^\circ$  as indicated by the dashed line. Once the optimal orientation  $\theta_1$  is found, one can follow the standard operation of a four-step phase recovery approach by recording intensity images corresponding to different phase shifts, e.g.  $\theta_2 = 0^\circ, 45^\circ, 90^\circ, -45^\circ$ .

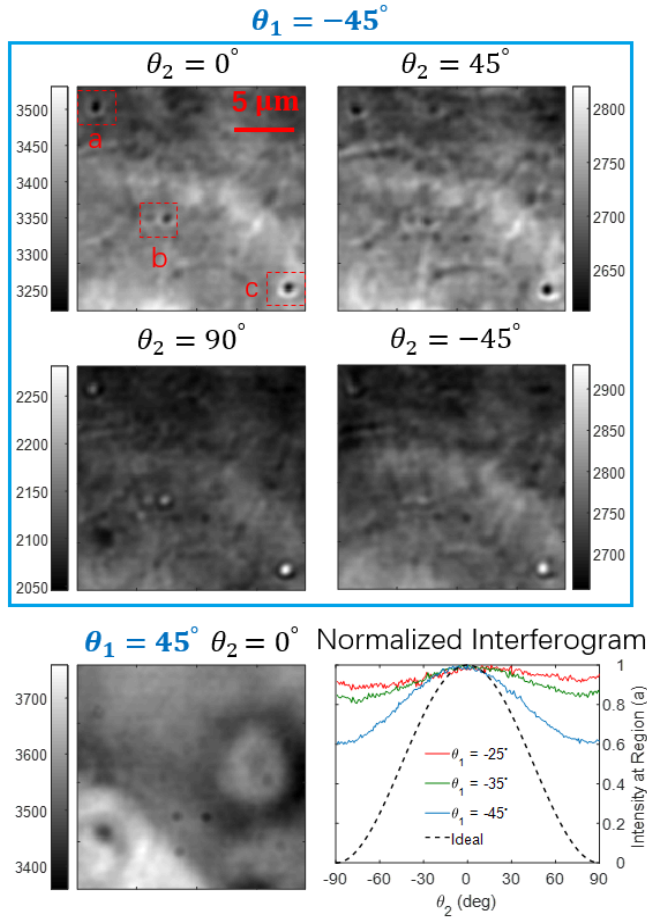


Figure 11: Measured intensities for phase-shifting method.

Phase and amplitude recovery using the phase-to-polarization encoding. Intensity distributions across a selected region of the sample for different orientations of two linear polarizers. Different in-focus regions containing scattering units are denoted by a,b,c. In these regions, the phase is recovered using the four intensity distributions corresponding to  $\theta_1 = -45^\circ$  and different values of  $\theta_2$  as illustrated in the blue box. Retrieving the amplitude of scattered field requires an additional intensity measurement of the reference field collected for  $\theta_1 = +45^\circ$  as shown on the bottom left. The bottom right panel shows the normalized interferograms (see text) corresponding to scattering unit a.

As seen in the recovered field images in Figure 12, a diffuse background is noticeable due to out-of-focus scattering units throughout the hydrogel volume. The in-focus subwavelength scattering units of interest are marked by the red boxes shown in Figure 12. We repeated fifty times

the four-step phase recovery procedure to generate an ensemble of measured fields. From these, we then evaluate the mean normalized amplitude  $\langle \bar{A}_s(\mathbf{x}) \rangle_i$  and phase  $\langle \phi(\mathbf{x}) \rangle_i$  together with the corresponding standard deviations  $\sigma_A(\mathbf{x})$  and  $\sigma_\phi(\mathbf{x})$  displayed in Figure 12.

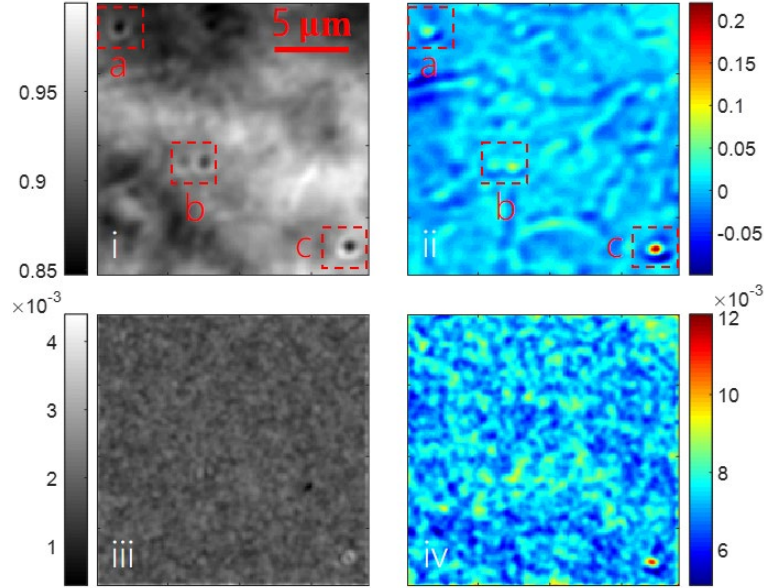


Figure 12: Results of full reconstruction of the scattered fields

(i) average of normalized amplitude  $\langle \bar{A}_s(\mathbf{x}) \rangle_i$ , (ii) average of phase  $\langle \phi(\mathbf{x}) \rangle_i$ , (iii) standard deviation of normalized amplitude  $\sigma_A(\mathbf{x})$ , and (iv) standard deviation of recovered phase  $\sigma_\phi(\mathbf{x})$  estimated over 50 different realizations of the measurement.

### 2.2.2 Subwavelength Sizing

We note that, in the amplitude images, all the in-focus scattering units are diffraction-limited and, therefore, their subwavelength physical sizes cannot be determined directly. However, it is evident that the influence of their physical sizes is still preserved in the phase distribution. This happens in subwavelength scattering because the phase, which is a dimensionless time delay

between the reference field and scattered field, is largely influenced by evanescent fields around the scatter and, therefore, is directly impacted by structural details at subwavelength scales [19].

Based on the measurement of the scattered field, one can now recover quantitative information about the morphology of the unresolved, subwavelength scattering centers. We recall that, in the subwavelength scattering regime, the phase of the scattered field is dominated by the volume and not the shape of the scattering object. This is the so-called ‘size effect’ [33]. Therefore, subwavelength clusters can be approximated to have spherical shapes and the corresponding diameter  $a$  can be obtained from the recovered phase provided that the refractive indices of clusters and background are known. As shown in Figure 13, a forward model based on Mie scattering could be developed in terms of the ‘phase time  $\Delta_\phi$ ’ [19], as opposed to a simple geometric delay  $\Delta_g$  determined by the linear thickness of a slab and the difference of retarded phase velocity.

We would like to emphasize that the elastic scattering by a subwavelength particle is not a simple wave retardation. It cannot be interpreted only in terms of propagating waves since the evanescent fields also play a major role in the transfer of energy [19]. Bound to the scattering center, the evanescent field stores and releases energy almost instantaneously, functioning as an ‘energy capacitor’ and, therefore, the measurable phase that characterizes the scattered field is not solely the phase velocity of the propagating wave. It follows that a phase inversion relying on  $\Delta_g$  is prone to produce erroneous results. This is further demonstrated in Figure 13.

Regions containing in-focus scattering units have been zoomed in, and their corresponding averaged phase  $\langle\phi(\mathbf{x})\rangle_i$  have been plotted in Figure 13. Even though these subwavelength scattering units have similar shapes in the amplitude images, their peak phases are significantly

different and contain the size information which can be inverted from the phase time  $\Delta_\phi$ . The vertical error bars denote the measured standard deviation of the recovered phases. An error estimation based on the optimal conditions for our camera with a pixel well capacity of  $31,900 e^-$  leads to a slightly lower value of 5.6mrad.

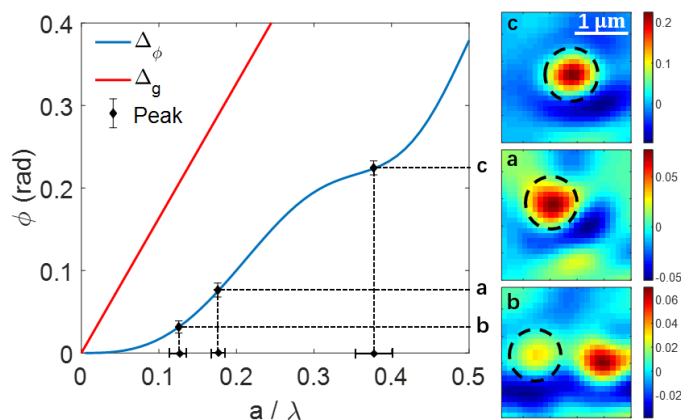


Figure 13: Relationship between the phase  $\phi$  and the diameter  $a$  of subwavelength particles.

The geometric delay  $\Delta_g$  and phase time  $\Delta_\phi$  are plotted for the case of polystyrene spheres in water and  $\lambda = 532 \text{ nm}$ . The displayed images represent the phase maps corresponding to the in-focus scattering units denoted by red boxes in Figure 12ii. For each of these, the physical size of the scattering object is estimated by mapping the peak phase within the dashed black circle through the size dependence of the phase time  $\Delta_\phi$ .

### 2.2.3 Comparison between Imaging Modalities

There are different approaches to characterize material structures with subwavelength resolution. Well-established fluorescence-based methods for subwavelength imaging rely on various means to localize different fluorescent markers [48]. For nanometer-scale localization, these approaches usually require SNR beyond thirty [49, 50, 51], which, in the context of shot noise limited detection, imposes a minimum number of emitted photons. Commonly, the emitting

photon flux is limited by optical saturation [52] and a minimum recording time is required to localize a marker with sufficiently high SNR.

The situation is quite different in elastic scattering where the scattered photon flux is limited only by the available photon flux in the incident field. Therefore, given sufficiently high incident flux, the sensitivity and temporal resolution are decoupled in this case. Elastic scattering approaches have been implemented in different common-path designs. For instance, interferometric methods relying on phase-shifting have been developed to characterize the elastically scattered fields [53]. In the case of subwavelength scattering, the performance is not optimal because the strengths of the reference and scattered fields are severely unbalanced.

Alternatively, one can measure interferometrically the extinction due to a scattering particle, localize its center of mass, and also estimate its size when the refractive index contrast is known a priori [54]. In principle, the ratio between the amplitudes of the incident and the scattered fields could be controlled by using an additional, partially reflecting interface, which, however, is difficult to adjust continuously during a measurement [55, 56].

The method presented here relies on phase-to-polarization encoding (P2P) and, for a given pixel well capacity, provides means to measure the scattered field with optimal sensitivity. The practical sensitivity is limited by the quality of polarization elements, which is not a fundamental limit for this concept. The experimental system is very robust and easy to adjust and, furthermore, it is prone to integration into a compact design. A number of further developments rely on the capability to recover both the phase and amplitude of the scattered field. Subwavelength sizing is just one such specific application. Other possible applications include backpropagation to recover

the structure of a source [57] or the size estimation of nanoparticles with unknown composition [33].

## CHAPTER THREE: SENSING IN MULTIPLE SCATTERING REGIMES

In this chapter, I will discuss sensing in multiple scattering regimes, where the interaction volume between light and matter is much larger than the case in subwavelength scattering. Although there are huge differences in the physical perspective, the scope is quite similar: information retrieval cannot be directly achieved by conventional intensity-based imaging approaches.

When a target is placed behind or embedded in random media such as fog, rain, or cloud, its emission is always accompanied by the emission from the random medium itself. The fact that both contributions are collected by the imaging system degrades the imaging quality by reducing both the contrast and the resolution.

If the target is self-luminous and placed behind a disturbing medium with small optical density (OD), the image can be phase-compensated by adaptive optics [58]. When the target functions as a secondary source by reflecting natural light, the imaging performance can be improved by using polarization [59], a priori information [60], and changes in OD [61]. All these scenarios are classified as ‘passive imaging’, since illumination cannot be controlled.

Taking advantage of controllable sources of illumination, imaging procedures can be augmented. ‘Active imaging’ approaches are more flexible and enable applications in dark environments such as night or deep water. In these circumstances, the imaging quality can be improved by simply choosing the appropriate wavelengths [62] or by direct time gating [63]. In this case, however, the detection ranges become limited by the power of illumination. A significant improvement in this respect can be brought by interferometric measurements and coherent processing [64] or, in other words, by taking advantage of the wave properties of light.

Nevertheless, modeling and optimizing such an imaging procedure poses significant computational challenges.

In most situations of interest, the macroscopic Maxwell equations are sufficient to describe the vectorial wave properties of light during light interaction with random media [65]. The controllable incident electromagnetic field can be regarded as a combination of plane waves, while the target and its surrounding random medium are regarded as complicated boundary conditions for the electromagnetic waves. Subject to these boundary conditions, each incident plane wave interferes with its corresponding wave scattered from the target and its environment. These waves scattered from random media are chaotic and unordered and lead to the ubiquitous ‘speckles’ [66]; this constitutes the so-called ‘coherent noise’ that degrades the performance of active imaging.

Simulating boundary conditions for realistic situations such as imaging through fog are prohibitive for current computational capabilities. One possible simplification is the radiative transfer approach [67], which treats random media statistically and uses concepts from classical radiometry and geometrical optics. The radiative transfer is widely applied for incoherent imaging [59, 60, 61, 63], but it can also provide a limited description of wave properties such as the second-order spatial coherence, which will be the first section of this chapter [68, 69]. When incident light is polarized, the scalar approximation of radiative transfer is not appropriate anymore [70, 71] and a so-called vector radiative transfer equation (VRTE) can be implemented [72].

Nevertheless, due to the inherent approximations involved, the use of VRTE is inadequate for many imaging applications. Firstly, the observer is required to be located in far-field of the random media [72], which rules out scenarios where both target and observer are embedded into the random medium. Secondly, the spatial distribution of the environmental particles is assumed

to be random and statistically homogeneous; their physical properties are estimated only as a result of an ensemble averaging [72]. Therefore, VRTE cannot account for speckle phenomena corresponding to specific spatial realizations of random media [73]. Lastly, in dealing with multiple scattering, the crossing connectors are neglected in the diagram of the dyadic correlation function (the ladder approximation) and, therefore, coherence effects such as enhanced backscattering cannot be accounted [74].

In the second section of this chapter, we present an approach for simulating the vectorial wave properties of light in the context of active imaging through random media, while reducing significantly the computational requirements. As a result, realistic imaging conditions can be effectively described.

### 3.1 Monte Carlo Simulation of Spatial Coherence Propagation through Random Media

Understanding light propagation in random media is important both for fundamental science and for practical applications. The research that greatly benefits from a proper description of light interaction with random media includes studies of light localization and coherent backscattering, deep tissue imaging, remote sensing, diffusing-wave spectroscopy, dynamic light scattering, imaging and telecommunication technologies etc. [75, 76, 77, 78]. Unfortunately, describing the multiple scattering of light in random media is a very difficult problem. Current approaches include perturbation analytical methods based on diagrammatic techniques [79], radiative transfer procedures [80, 81], and exact numerical techniques such as T-matrix [82], finite difference and finite elements [83] or discrete dipole approximation [84]. Analytical approaches are limited only to simple geometries and/or to weakly scattering media. Most of the numerical

methods are constrained by the current development level of the computer technology and usually unsuitable for modeling objects with dimensions larger than 10 wavelengths; also, they are very inconvenient for modeling phenomena involving partially coherent light.

The radiative transfer equation (RTE) provides a reasonable compromise between accuracy of simulation and computational speed. Previously, RTE was successfully used for the description of both tenuous (atmospheres, ocean) and dense (papers, photographic emulsions etc.) media [81]. One of the common approaches to solve RTE is the Monte Carlo (MC) technique [85, 86]. To solve RTE, the MC applies a ray-tracing approach where each ray represents a fraction of the light energy, which can conveniently be regarded as a “photon”. Photons are launched into the random medium characterized by scattering and absorption lengths and experience a random walk, which develops by cascading successive steps of interaction. For each event, the step size and its direction are independently determined by the physical properties of random medium. The path of a photon is ended when its intensity reaches a lower threshold or when it exists the scattering medium. Physical quantities such as energy, position, direction, path length, and number of scattering events, are recorded for each photon. By tracking a sufficient number of photons, one can estimate a variety of global physical quantities like intensity distribution, reflection and transmission coefficients, bidirectional reflectance distribution function (BRDF), polarization characteristics [87, 88, 89]. Note that all these properties are determined by measurements performed at one single location, i.e. they are single point properties.

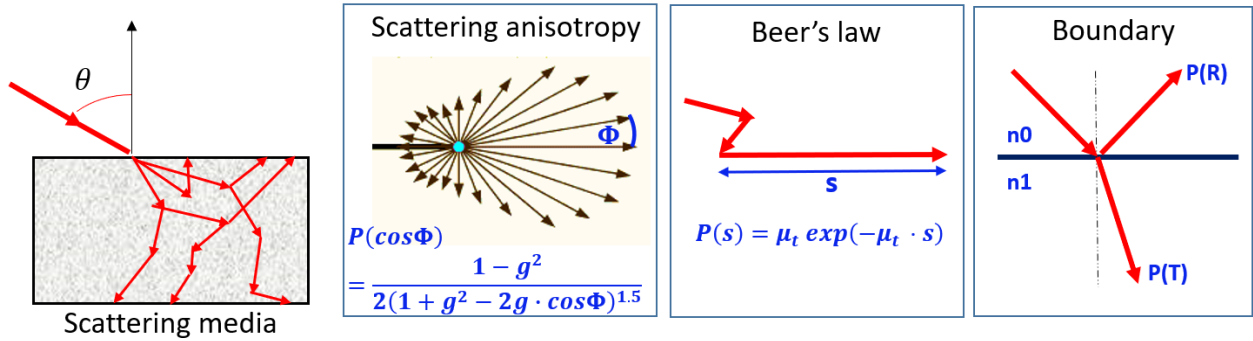


Figure 14: Traditional Monte Carlo simulation of light propagation in scattering media.

Nevertheless, two-point field characterization provides much richer information about field properties. An important two-point characteristic is the spatial coherence function (SCF), which is defined for a scalar quasi-monochromatic field as [90]

$$\Gamma(\mathbf{r}_1, \mathbf{r}_2) = \langle E(\mathbf{r}_1)E^*(\mathbf{r}_2) \rangle, \quad (5)$$

where  $\mathbf{r}_1$  and  $\mathbf{r}_2$  are the two observation points and  $E(\mathbf{r})$  is the complex electric field. The angular brackets indicate an ensemble average over all possible realizations of  $E(\mathbf{r})$ .

If one attempts to use MC techniques for describing coherence properties such as  $\Gamma(\mathbf{r}_1, \mathbf{r}_2)$ , the procedure must be modified to permit quantifying the extent of correlations between the field at two different spatial locations. One such modification, named Coherent Monte Carlo, was suggested to investigate the coherent photon transport in a series of papers devoted to the theoretical description of optical coherent tomography (OCT) [91,92]. In this approach, the propagating light is represented by a plane wavelet with its propagation direction and path length determined by the Monte Carlo technique and with the scattering computed using the Mie theory. However, only the ballistic component of light transport was of interest in OCT.

Aside from these OCT related developments, several attempts were also made to extend the application of MC to the case of partially coherent light [93]. In these approaches, the phase information was attached to the photons propagating in a multiple scattering environment. Based on the Huygens–Fresnel principle, interference and diffraction phenomena for simple diffraction problems were implemented using Monte Carlo in [94, 95]. Similarly, the spatial coherence of light in free space propagation was described in [96]. Each point on a wavefront in [96] was considered to be a source of cylindrical wave (known as a Huygens wavelet) emanating from that point. Monte Carlo sampling of the Huygens wavelets involved launching multiple rays from the center of each wavelet and tracking the change in phase of each ray before it reaches the observation plane. A partially coherent source field was created by using multiple Huygens wavelets emanating from different points across a given source realization. At the observation plane, rays were added coherently to form final field in [97], the above approaches are extended to the studies of coherence propagation through thin slabs of scattering tissue. Coherent properties of the source together with photons phases were taken into account in the Monte Carlo method discussed in [98]. However, the simple procedure of adding phases to the photon paths is debatable [99]. In particular, it was noticed in [99] that energy conservation law is violated and the detected energy depends on the discretization of observation area.

An alternative description of coherent photon transport in a turbid medium was suggested in [100] by introducing certain decoherence models in the Monte Carlo calculations without explicitly attempting to calculate relevant phase variation of photons. One another Monte Carlo algorithm was suggested in [101,102] based on the integral form of Helmholtz equation. This approach allowed calculating the coherent field distribution for a fixed collection of scatterers.

In this section, we demonstrate an alternative Monte Carlo procedure. We will show that coherent phenomena can be described based on numerical solutions of the radiative transfer equation for the specific intensity (Wigner function) [103, 104]. By incorporating a Wigner transformation in the Monte Carlo technique, we are able to study the propagation and the transformation of spatial coherence function in a variety of scattering media.

### 3.1.1 Wigner Monte Carlo Method

Our aim is to describe the transformation of the SCF while partially coherent light propagates through a scattering medium. One possible approach uses the radiative transfer equation and solves it for the specific intensity  $I(\mathbf{r}, \mathbf{u})$ , where  $\mathbf{u}$  determines the direction of energy flow at the location  $\mathbf{r} = (\mathbf{r}_1 + \mathbf{r}_2)/2$  [105]. The local coherence properties of the field incident on the random medium can then be related to the angular distribution of wavevectors through the Wigner's transform [104]:

$$I_I(\mathbf{r}, \mathbf{u}) = \left(\frac{k}{2\pi}\right)^2 |u_z| \int \Gamma(\mathbf{r}, \boldsymbol{\rho}) \exp(-ik\rho_\perp u_\perp) d^2\rho_\perp. \quad (6)$$

Here  $\boldsymbol{\rho} = \mathbf{r}_2 - \mathbf{r}_1$ ,  $\rho_\perp$  is the distance between two observation points along the wavefront (perpendicular to the incident wave-vector  $\mathbf{k}_I \parallel \hat{z}$ ),  $\mathbf{u} = (u_\perp, u_z)$  is a unit vector with corresponding components along ( $\mathbf{u}_z$ ) and perpendicular ( $\mathbf{u}_\perp$ ) to the wavefront propagation. The specific intensity  $I_I(\mathbf{r}, \mathbf{u})$  determines the directions and weights of the ‘photons’ that are launched into the random medium during Monte Carlo procedure.

Similarly, all the directions and weights of the ‘photons’ leaving the random medium can be collected to generate the specific intensity of the scattered field  $I_S(\mathbf{r}, \mathbf{u})$  from which the SCF of the scattered field can be evaluated as:

$$\Gamma_S(\mathbf{r}, \boldsymbol{\rho}) = \int I_S(\mathbf{r}, \mathbf{u}) \frac{\exp(ik\rho_{\perp}u_{\perp})}{|u_z|} d^2u_{\perp}. \quad (7)$$

The calculation of spatial coherence function is greatly simplified in a case of homogeneous partially coherent wavefronts. In this case, all the points of the scattered wave are equivalent  $I_S(\mathbf{r}, \mathbf{u}) \equiv I_S(\mathbf{u})$  and in Eq. (7) one can simply assume that all the scattered ‘photons’ emerge from the same point.

For finite partially coherent beams, the angular distribution of wavevectors and the corresponding spatial coherence of the output field should be evaluated locally. In plane-parallel geometries, if the coherence function does not change across the input beam, the net local output in the space of directions  $\mathbf{u}$  is the convolution between the intensity profile  $I_I(\mathbf{r})$  of the input beam and the impulse response  $I_{ir}(\mathbf{r}, \mathbf{u})$  of the system:  $I_S(\mathbf{r}, \mathbf{u}) = \int I_I(\mathbf{r}') I_{ir}(\mathbf{r} - \mathbf{r}', \mathbf{u}) d\mathbf{r}'$ .

The impulse response of the system  $I_{ir}(\mathbf{r}, \mathbf{u})$  can be evaluated as the distribution of the directions of energy flow across the whole output surface created by a small patch of a wavefront (Figure 15).

In short, the overall Monte Carlo simulation procedure is followed like this. For an input beam with a given spatial coherence  $\Gamma(\mathbf{r}, \boldsymbol{\rho})$ , the corresponding specific intensity is calculated according to Eq. (6). This specific intensity is then sampled by a large number of ‘photons’ that propagate in a scattering medium as in usual Monte Carlo procedure. Finally, the SCF at the output is then reconstructed using Eq. (7).

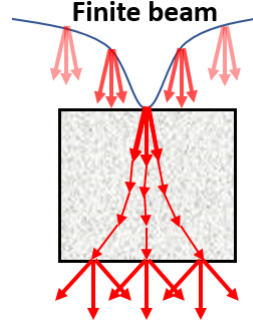


Figure 15: The geometry of spatial coherence propagation.

A beam with a Gaussian intensity profile propagates through a random medium. Randomization of photons' directions due to scattering leads to the deterioration of spatial coherence. The distribution of the scattered photons over locations  $r$  and directions  $u$  along the output surface created by a small source at input surface forms the impulse response of the slab.

### 3.1.2 Numerical Simulation

As an example of application of the proposed Monte Carlo techniques, we considered the transmission of a Gaussian beam through a plane-parallel slab of scattering medium (Figure 15). This problem was solved previously in a small scattering angle approximation to the radiative transfer equation [106, 107]. In particular, the following expressions were found in [106]:

$$\Gamma_s(r, \rho_\perp, z) \propto \int_{-\infty}^{\infty} dq \exp(iqr) \exp[-I_1(\rho_\perp, q, z)] I_0(\rho_\perp, q, z), \quad (8)$$

where

$$I_1(\rho_\perp, q, z) = \mu_T z - \frac{N\sigma_N\sqrt{\pi}}{\theta_0 q} \left\{ \operatorname{erf}\left(\frac{k\theta_0}{2}\rho_\perp\right) - \operatorname{erf}\left[\frac{k\theta_0}{2}\left(\rho_\perp - \frac{zq}{k}\right)\right] \right\},$$

$$I_0(\rho_\perp, q, z) = \frac{1}{2\pi} \exp\left[-\frac{\left(\rho_\perp - \frac{qz}{k}\right)^2}{4a^2} - \frac{a^2 q^2}{4}\right].$$

Here  $\mu_T$  is the total extinction coefficient,  $N$  is the number density of colloidal particles making up the scattering medium,  $\sigma_N$  is the scattering cross section integrated over near-forward angles,

$\theta_0$  is the  $1/e$  half-width of near-forward scattering peak estimated from the Mie scattering function,  $k$  is the wavenumber.

As SCF is very sensitive to the local distribution of ‘photon’s’ propagation angles, one needs to describe the scattering events in the medium as precisely as possible. For media with spherical scatterers used in our calculations below, the angular distribution of scattered radiation is well characterized by Mie theory. Hence, in MC calculations we used the exact Mie scattering phase function instead of more commonly used Henyey-Greenstein scattering function (Figure 16). A third party MATLAB code was used for calculation of Mie scattering functions [31] based on theoretical approach of Bohren and Huffman [15]. The probability of scattering into a certain angle was calculated numerically according to procedure described in [108,109] called inverse transform sampling. First, a cumulative distribution function (CDF) was constructed based on Mie scattering phase function. Then, the  $CDF(\theta)$  was interpolated to allow for an even sampling from zero to one, thus generating a lookup table for the conversion from uniformly distributed random number to the scattering angle  $\theta$ . In our simulations, a  $10^7$  elements lookup table was generated to properly sample lobes of Mie scattering function (Figure 16).

For numerical simulations, the Monte Carlo code was implemented in MATLAB with the parallel computing toolbox and double precision computation accuracy. The simulations were run on a 6 core CPU (Intel Xeon E5-2630 v2, 2.60 GHz, 128 GB RAM). One million photons have been generated for sufficient sampling of specific intensity  $I_S(\mathbf{r}, \mathbf{u})$ , and the bin size has been set as  $3.6 \mu\text{m}$  for convolution. For a typical scattering experiment, it takes only a few seconds to finish the simulation using one million photons. We should note that the time complexity in our MC

method is quite close to the existing MC models. The main difference in our method is processing of the directional information of photons described by Eq. (7).

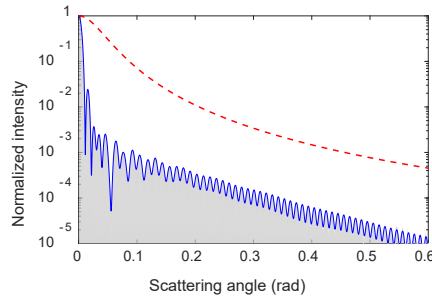


Figure 16: Comparison between Mie (blue solid line) and Henyey-Greenstein (red dashed line) scattering phase functions.

Even though the asymmetry parameter in both cases is the same,  $g = 0.955$ , the fine details of intensity angular distribution are very different. The gray area shows the histogram of scattering angles generated from the lookup table.

We compared the predictions of Eq. (8) with MC calculations in the case of a coherent Gaussian beam with wavelength  $\lambda = 632\text{nm}$  and  $140\mu\text{m}$  waist that impinges at normal incidence on the surface of a scattering medium. The medium contained a number density  $N = 3.9 \times 10^5 \text{cm}^{-3}$  of scatterers dispersed in a matrix with a refractive index  $n_0 = 1.42$ . The scatterers are  $46 \mu\text{m}$  polystyrene particles. Let us note that for particles with dimensions much larger than a wavelength, the scalar theory (5) is well applied to the problem in question [110]. Particles have scattering cross section  $\sigma_s = 3.47 \times 10^{-5} \text{cm}^2$ , and an asymmetry parameter  $g = 0.955$  which corresponds to the nearly forward scattering. The corresponding scattering mean free path  $l_s = 1/\mu_T = 740\mu\text{m}$ . The corresponding Mie scattering phase function is shown in Figure 16. One can see that for the same asymmetry parameter  $g$ , the Mie and Henyey-Greenstein phase scattering functions have very different shapes. We will show later that this results in very different predictions of coherence properties.

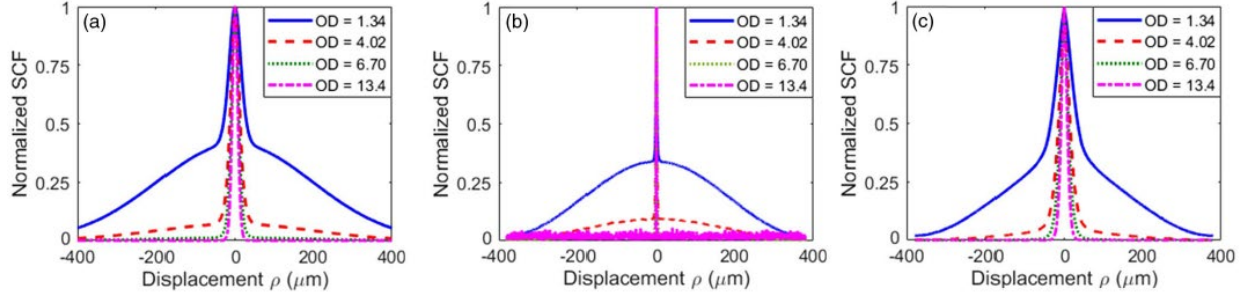


Figure 17: Normalized SCF at the output of scattering media containing nearly forward scattering particles for different optical densities (OD).

(a) Calculations performed based on the near-forward scattering approximation using Eq. (8); (b) results obtained from Monte Carlo procedure when using Henyey-Greenstein scattering phase function; (c) results based on Monte Carlo procedure when using Mie scattering phase function.

Figure 17 shows typical results for SCF evaluated on a back side of plane-parallel slab (Figure 15) and normalized to the maximum of intensity. The results correspond to a Gaussian beam propagating through media with different optical densities (OD)  $L/l_s$  with  $L$  being the thickness of the medium. SCF is measured at the center of the Gaussian beam  $\mathbf{r} = 0$ . One can notice good quantitative agreement between the predictions of small angle scattering approximation [106] and our Monte Carlo numerical experiment (Figure 17 a,c). However, the relative difference between these two results can reach 30%. The narrow peak in the middle corresponds to the multiply scattered light while the wider pedestal is determined by unscattered ballistic light. As expected, the coherence length of the transmitted field decreases with increasing the thickness of the scattering slab, which corresponds to increased amount of scattering events.

Figure 17(b) shows the results of Monte Carlo simulations obtained with the approximate Henyey-Greenstein scattering phase function. Comparing it to Figure 17(c), one can see that the

Henye-Greenstein function leads to a very different result. This drastic distinction is due to the much wider forward scattering lobe of the Henye-Greenstein function (Figure 16) that makes the photons deflect into larger angles. According to Eq. (7), this results in a lower coherence of the central peak.

The progression of the width of the central peak with the geometrical thickness  $L$  can be qualitatively understood. During each scattering event, light deflects by angle  $\theta_0$  from its original propagation direction. The average deflection at the output  $\Delta\theta_{out}$  is determined by the average number of scattering effects  $N_s$  which can be easily estimated in the Monte Carlo simulations

$$\Delta\theta_{out} = N_s\theta_0. \tag{9}$$

The coherence length of the field at the output is related to  $\Delta\theta_{out}$  by Eq. (7). Table 1 compares the results of this rough estimation to the exact Monte Carlo results and, as can be seen, Eq. (9) provides a rather good estimation of the coherence length.

Table 1: The full width at half maximum (FWHM) of the spatial coherence function estimated from different approaches.

Optical Density	Number of Scattering Events	Coherence length estimated from Eq.(8) (um)	Coherence length estimated from MC (um)	Coherence length estimated from Eq.(9) (um)
1.34	1.5	59.8	68.4	63.9
4.02	4.5	27.2	29.7	29.0
6.70	7.5	20.8	22.1	21.9
13.4	15.5	16.4	16.4	14.1

Contrary to the approach in [106], our Monte Carlo method can operate beyond the near-forward scattering approximation. In this respect our method permits calculating the SCF even for the light scattered backwards from random medium. For instance, in Figure 18 we show the results

of these calculations for the back-reflected light for the same parameters as in Figure 17. We would like to comment on several interesting details of these results. First, the coherence length of the back-scattered light is narrower than in the case of the transmitted light. Second, one can observe rather counter-intuitive result in Figure 18: increasing the thickness of colloidal slab decreases the magnitude of central peak, which is determined by multiple scattering. This can be explained by the fact that the amplitude of the forward scattering for  $46\mu\text{m}$  colloidal particles used in these tests is  $\sim 10^4$  times larger than that of back-scattering. Thus, the central narrow peak for the thin colloidal sample is determined mainly not by backscattering from colloidal particles, but by forward scattering of light reflected from a back surface of plane-parallel slab. For thick samples this forward scattering becomes dispersed over large area and its effect in the central peak decreases.

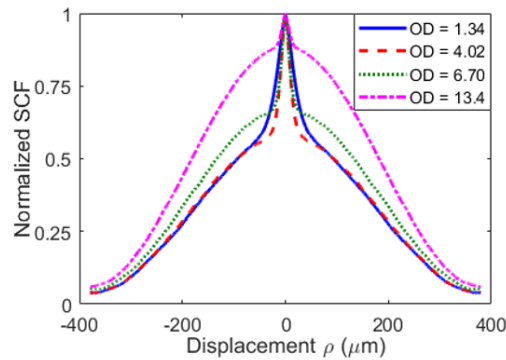


Figure 18: Normalized SCF for the reflected light.

The parameters of the scattering medium are the same as in Figure 17.

### 3.1.3 Non-Line-of-Sight Imaging

Imaging systems map spatially the distribution of light across an object onto a distant observation plane for further recording and processing. Of course, when objects are too distant or too small to be satisfactorily described by an imaging system, only unresolved sensing is available for estimating physical properties of the object. Whether the object is actively illuminated in a controlled manner, or it is self-luminous, or it is subject to some passive ambient lighting, the imaging procedure is typically constrained by the need for direct view to the object [111].

In non-line-of-sight conditions, an ideal “specular” reflector such as a mirror preserves most of the light properties, including the wavefront, and the imaging procedure is similar to the direct line-of-sight case. Decreasing the mirror’s specularity hinders this capability. A shattered mirror alters the directionality of reflected light and, as a result, only a distorted version of the image can be transferred as illustrated in Figure 19. The blur can be mitigated if the disturbance can be quantified. Unfortunately, because of the random nature of surface scattering, there are no simple deterministic approaches like ray tracing or conventional diffraction theories to describe the relationship between the incident and reflected optical fields. The situation is further complicated if the light is redirected by a diffusing wall when the interaction is not limited to the surface of the random medium but it extends throughout its volume. In these conditions, recovering the incident wavefront is challenging. The complicated process can be described in terms of the associated transfer matrix, which can be found by controlling the properties of radiation before and after the scattering medium [112, 113, 114, 115, 116, 117].

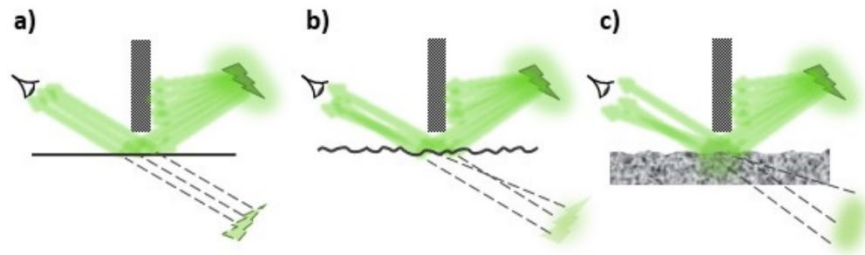


Figure 19: Different non-line-of-sight sensing conditions.

(a) A perfect reflector permits imaging around the corner. (b) A broken mirror alters the optical wavefront and impedes forming a clear image. (c) A random medium will alter the reflection even more due to both surface and volume scattering contributions.

Nonetheless, some these limitations can be alleviated by an active control of the illumination source. For instance, one can employ time-of-flight approaches to gate the time necessary for light emerging from a controllable source to first reach an object and then a detector capable of discriminating the transient time [118, 119]. Imaging angularly small targets hidden around a corner is also possible when using additional measurements performed on reference objects [120] or when the scene is illuminated with temporally coherent light [121, 122, 123, 124]. Sometimes, when an object is diffusively illuminated by a laser and its reflection generates a non-uniform intensity distribution across the scattering wall, detecting the evolution of this intensity allows tracking the object's movement [125, 126].

Unfortunately, the sensing conditions are significantly more restrictive when one does not have access to the source of illumination. If the object does not generate intensity variations that can be measured, one cannot reconstruct an image in the conventional intensity-based sense [111]. However, even in this rather limiting situation, the object itself acts as the primary (if self-luminous) or the secondary source of partially coherent radiation and relevant information about the object is

carried by the statistical properties of the radiated field. The remaining practical question is: do these field properties survive the interaction with scattering obstructions?

In the following, we will demonstrate that spatial correlations of the electromagnetic field can be transferred between the incident and reflected fields in spite of the random nature of interaction with a multiple scattering medium. Specifically, we will show that scattering from randomly inhomogeneous media does not completely destroy the spatial coherence of radiation. This means that a multiple scattering wall can act as a “broken mirror” for spatial coherence and its distortions can be partially mitigated. We demonstrate that this effect permits retrieving information about the size and shape and allows determining the location of an object even in non-line-of-sight situations.

We consider the situation where radiation from an incoherent source (target) reflects off a scattering surface, e.g. a painted wall, and propagates further until it reaches a detector, which can measure its spatial coherence function (SCF)  $\Gamma(\mathbf{r}, \mathbf{s}) = \langle E(\mathbf{r} + \frac{\mathbf{s}}{2}) E^*(\mathbf{r} - \frac{\mathbf{s}}{2}) \rangle$ . Here,  $E(\mathbf{r})$  is the electric field at the location  $\mathbf{r}$  and  $\mathbf{s}$  is the distance between the points for which the field similarity is being measured (shear).

It is well known how spatial coherence evolves in free-space propagation. Thus, certain information about the source can always be extracted by measuring the coherence of the light at distant locations [127]. However, upon reflection from a scattering medium, it is expected that SCF is affected in a way that may complicate this reconstruction procedure. Let us examine the general situation of partially coherent light incident onto a scattering medium as shown in Figure 20. Intuitively, one can anticipate that the coherence degrades due to the additional randomization

of light and the information about the source of light deteriorates. To mitigate the influence of this interaction, one needs to understand how the coherence properties transform during reflection.

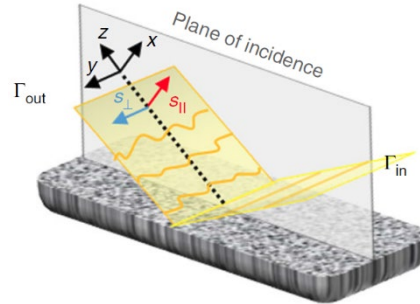


Figure 20: Schematic representation of the field reflected from a diffusive wall and its SCF assessed for in-plane  $s_{||}$  and out-of-plane  $s_{\perp}$  shears.

### 3.1.4 Spatial Coherence after Surface and Volume Scattering

The transformation of SCF in reflection is well understood only for homogeneous, plane-parallel interfaces [128]. Earlier studies also addressed, to a certain degree, the phenomenology of coherence degradation but only in transmission through inhomogeneous media [129, 106]. In the previous sections of this chapter, Monte Carlo technique permits estimating the transformation of spatial coherence function in multiple scattering media [68]. To treat the reflection from realistic scattering media, we augmented this method with a proper description of the surface roughness.

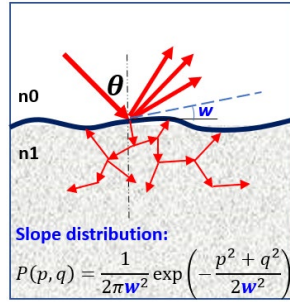


Figure 21: Spatial coherence and wall interpreted by Wigner Monte Carlo method

For the reflection regime, spatial coherence is affected by both the scattering media (volume scattering) and rough surface (surface scattering). We made three assumptions to simplify the interaction between light and a rough surface [130]. First, when the surface is locally smooth, a wave can be described using a ray (tangent plane approximation). Second, the surface profile is described statistically (statistical approach sufficiency). Third, surface self-shadowing and multiple scattering are neglected. Thus, rough surface is simplified to a Gaussian statistical slope distribution. This statistical slope randomizes the directions of incoming rays; thus, the distribution of generalized radiance becomes more diverse, and the spatial coherence function is narrowed. To summarize simply, surface scattering can also be interpreted in a statistical ray manner, which is consistent with Monte Carlo simulation for volume scattering. Although natural surfaces should not necessarily satisfy all our assumptions, we found that the conclusions of Monte Carlo simulations describe very well the experimental situations described in the following.

Monte Carlo simulations show that light reflected from inhomogeneous media can be effectively described as the superposition of a multiple-scattering component originating in the bulk and the single scattering at the surface. We found that for typical painted walls the volume scattering randomizes significantly the set of directions  $\mathbf{u}$  corresponding to the incident field and,

according to Eq. (7), the coherence information carried by this component is severely altered or even destroyed. However, the inherent single scattering at the surface of any diffusive wall leads to a much smaller randomization of the field, as we will show later.

For the Monte Carlo simulations of volume scattering, we used typical parameters of white paints: TiO<sub>2</sub> particles with a diameter 200 nm, refractive index 2.6763, and a fractional volume 10% distributed in a matrix with refractive index 1.5. The thickness of the simulated layer is 0.6 mm. We found that the Kirchhoff approximation for the description of surface roughness and a Gaussian distribution of the local slopes [131] allows both a simple Monte Carlo implementation and a satisfactory description of experimental results. The mean surface slope was determined by matching the outcome of the Monte Carlo simulation to the measured SCF of reflected light for different angles of incidence ranging from 50° to 80°. From the small value of the slope variance (70 mrad) obtained from the fitting one can conclude that for these materials the shadowing effects are insignificant [132].

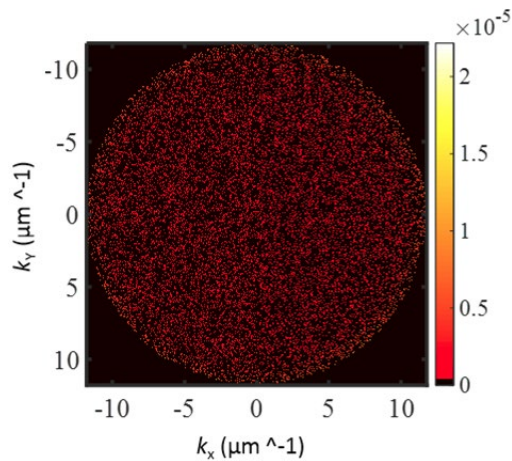


Figure 22: Distribution of generalized radiance for volume scattering.

The Monte Carlo simulations uncovered several features of scattering. First, even though the volume scattering happens in a thin subsurface layer (0.6 mm), the corresponding average number of scattering events is rather high (approximately 500 scattering events on average for chosen set of parameters). This leads to a complete randomization of volume scattered light with rays of reflected light uniformly distributed along all directions, as shown in Figure 22. Thus, randomized volume scattering does not carry any useful directional information and leads to the light completely losing its coherence properties.

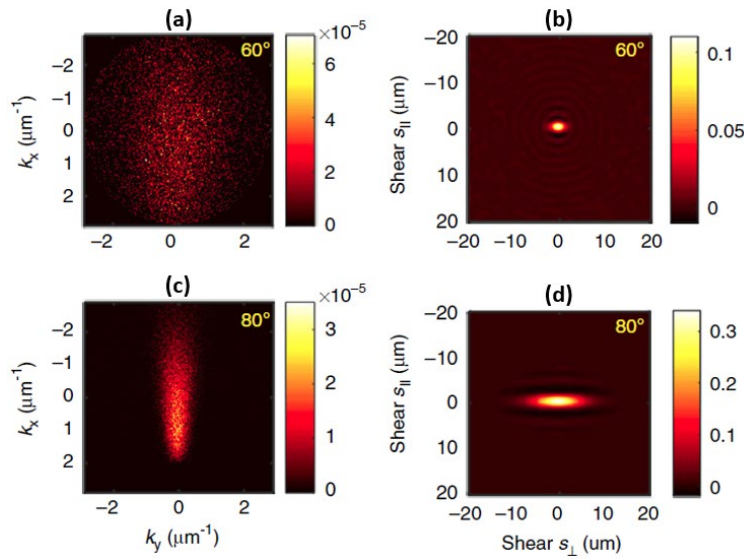


Figure 23: Anisotropic transfer of spatial coherence.

(a) and (c) Angular distributions of specific intensity corresponding to 60o and 80o angle of incidence, respectively. (b) and (d) Corresponding degrees of the spatial coherence. The incident light is fully coherent spatially and the coherence function of the output is evaluated next to the surface. Parameters of the scattering medium are indicated in the Methods. The mean slope of surface roughness of the simulated medium is  $\sigma = 0.07$  rad.

Second, the randomization of the light scattered from the surface is determined by the mean slope. In general, the randomization of wave vectors occurs differently for the components in and

normal to the incidence plane. With the increase of the incident angle, the randomization of the component normal to the plane of incidence decreases, as shown in Figure 23. Hence, for grazing angles the spatial coherence for shears normal to the plane of incidence survives much better than for shears in the plane of incidence.

Third, energetically speaking, volume scattering usually dominates the surface scattering for incidence angles close to the normal (Figure 24). For a larger incident angle, the ratio of surface scattering over volume scattering increases. In other words, the informationally deprived ‘noise’ from volume scattering decreases as the incident angle increases. It is more practical to view the comparison between surface and volume scattering using the energetic density in the wavevector space. The volume scattering is more or less uniformly distributed over  $2\pi$  solid angle (Figure 22). Surface scattering is distributed over much smaller angular range and concentrated along specular direction of reflection. Therefore, the energetic density in wavevector space is dominated by surface scattering when observing in the direction of specular reflection.

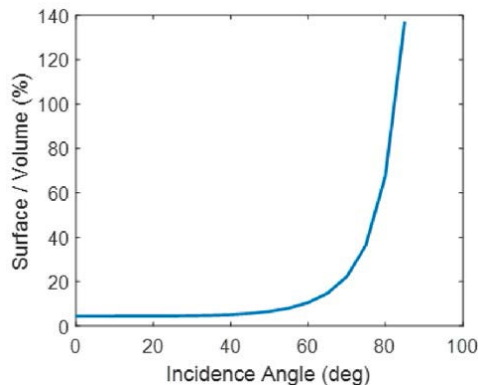


Figure 24: Monte Carlo simulation for energy ratio between surface scattering and volume scattering.

The contribution of volume scattering can be suppressed even more if the field-of-view (FOV) of the detection device is limited to the angles occupied by wave vectors carrying useful information (Figure 25). The finite size FOV effectively truncates the significant part of volume scattering, which causes surface scattering to dominate (Figure 25 b). Thus, the reflection from a highly scattering medium can be reduced to the reflection from a rough surface – broken mirror.

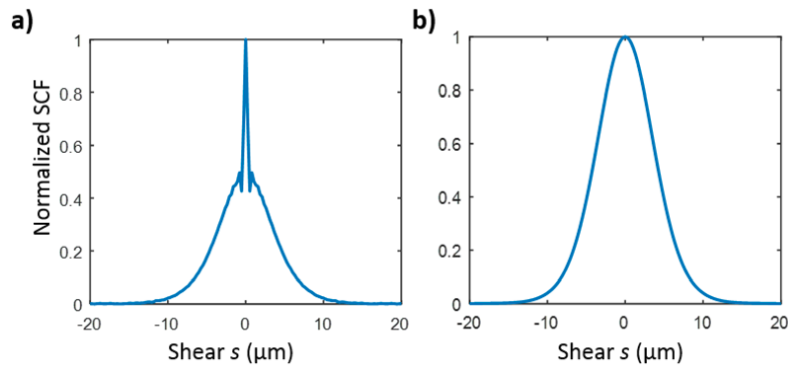


Figure 25: Spatial coherence function measured for different field of view.

(a) SCF for the large field of view observation; (b) SCF for a restricted FOV.

Therefore, the coherence function is obtained from the specific intensity using Eq. (7) and, as can be seen in Figure 23(b) and Figure 23(d), its extent is rather limited spatially. But, most interestingly, the coherence degradation process is not isotropic. We find that, perpendicular to the scattering plane, the spatial coherence  $\Gamma(s_{\perp})$  survives much better than for in-plane  $s_{\parallel}$  shears. In fact, this difference between the two corresponding coherence lengths,  $l_c^{\perp}$  and  $l_c^{\parallel}$ , increases with the angle of incidence, which is an effect closely related to the ‘glitter path’ phenomenon: the elongated reflection of a low Sun or Moon on the water’s surface. In this case, the angular spread of wavevectors is determined by the angle of incidence  $\theta$  and the properties of the rough surface

[133, 134]. From the Wigner transformation in Eq. (7), one can then infer the coherence length  $l_c^\perp \propto (\sigma \cos \theta)^{-1}$ .

Although natural surfaces should not necessarily satisfy all our assumptions, we found that the conclusions of Monte Carlo simulations describe very well the experimental situations described in the following. Monte Carlo simulations for the transformation of spatial coherence in reflection were performed for a scattering medium corresponding to a typically painted surface. Typical parameters of white paints (TiO<sub>2</sub>) were used: inclusion particles diameter of 200 nm, the refractive index of particles is 2.67, the refractive index of the matrix is 1.5, the fractional volume of inclusions is 10%, the surface mean slope is 70 mrad (this value was estimated from the fitting to experimental data), and the thickness of simulated slab is 0.6 mm.

We analyze this effect in detail using both Monte Carlo simulations and the complex-valued SCF measurements using the Dual Phase Sagnac Interferometer (DuPSaI) procedure [135]. A typical example of measured SCF for reflection from a diffusive wall (estimated transport mean free path 0.9 μm) is presented in Figure 26(a) showing a significant difference between in-plane and off-plane shears. Moreover, in Figure 26(b) one can clearly see the monotonic behavior of  $l_c^\perp$  over a significant range of angles of incidence  $\theta$ . The fact that, in certain conditions, the spatial coherence survives in spite of the medium's diffusiveness can be used to recover information about the source even in non-line-of-sight circumstances.

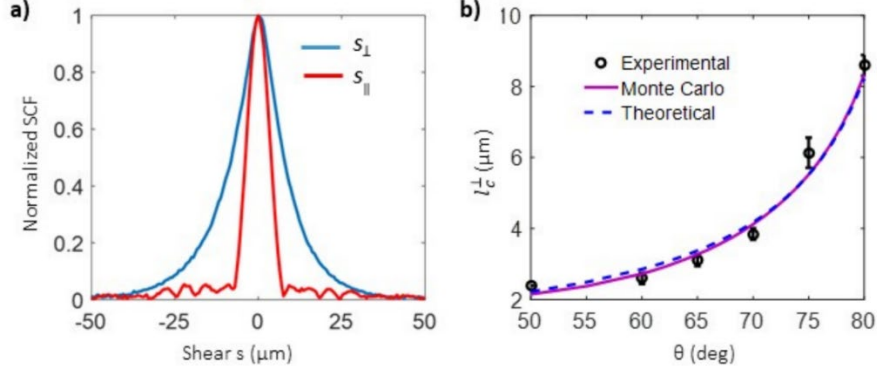


Figure 26: “Glitter path” effect in reflection from random media.

(a) Experimental values of the normalized spatial coherence for in-plane  $s_{\parallel}$  and off-plane  $s_{\perp}$  shear corresponding to  $80^{\circ}$  incidence angle. (b) Experimental and simulated values of the off-plane coherence length  $l_c^{\perp}$  as a function of the angle of incidence  $\theta$ . Both the source and detection system are located 1m away from the multiple scattering wall. The solid line represents the Monte Carlo fit to the experimental data from which the average slope of the surface roughness was estimated to be  $\sigma = 0.07$  rad. The dashed line is the corresponding analytical expression  $l_c^{\perp} \propto (\sigma \cos \theta)^{-1}$ . The coherence length (half-width at half-maximum of SCF) of the field incident on the wall is  $132\mu\text{m}$ . The error bars were calculated by repeating the measurement and calculating coherence length  $l_c^{\perp}$  for all the measurements.

### 3.2 Vector Wave Simulation of Active Imaging through Random Media

Nowadays, lasers are widely used in active imaging through random media [8], thus it is very meaningful to build a forward model which can describe every aspects of vector field. Since it is computationally expensive to simulate real scenarios like fog and rain, this section will help minimize the computational complexity.

#### 3.2.1 Statistical Equivalence

As shown in Figure 27(a), the target is embedded in an infinitely wide random medium of thickness  $z$ . In response to an incident plane wave  $\mathbf{E}_i(\mathbf{r})$ , the scattered wave  $\mathbf{E}_s(\mathbf{r})$  contains contributions from both the target and the medium itself. In other words, both the target and the

surrounding random medium are secondary sources, as shown in Figure 27(b). The total field  $\mathbf{E}_{tot}(\mathbf{r})$  everywhere is the interference between  $\mathbf{E}_i(\mathbf{r})$  and  $\mathbf{E}_s(\mathbf{r})$ , and the relation between  $\mathbf{E}_i(\mathbf{r})$  and  $\mathbf{E}_s(\mathbf{r})$  is determined by volume integral equation [65]:

$$\mathbf{E}_s(\mathbf{r}) = k_0^2 \int_V [m^2(\mathbf{r}') - 1] \vec{G}(\mathbf{r}, \mathbf{r}') \cdot [\mathbf{E}_i(\mathbf{r}') + \mathbf{E}_s(\mathbf{r}')] d^3\mathbf{r}', \quad (10)$$

where the integral extends over a volume  $V = V_t \cup V_r$  comprising both the volume  $V_t$  of the target and the volume  $V_r$  occupied by the particles inside the random media. In Eq. (10),  $k_0$  is the wave number in the host medium,  $m(\mathbf{r}')$  is the refractive index of the target and particles relative to the host medium, and  $\vec{G}(\mathbf{r}, \mathbf{r}')$  is the free space dyadic Green's function.

The scattered field  $\mathbf{E}_s(\mathbf{r})$  can be further separated into two classes: emission from the target  $\mathbf{E}_{st}(\mathbf{r})$  and that from random medium  $\mathbf{E}_{sr}(\mathbf{r})$ :

$$\mathbf{E}_s(\mathbf{r}) = \mathbf{E}_{st}(\mathbf{r}) + \mathbf{E}_{sr}(\mathbf{r}) \quad (11)$$

In this way, the total field  $\mathbf{E}_{tot}(\mathbf{r})$  at any position  $\mathbf{r} \in V_t \cup V_r$  of the secondary source is the interference between  $\mathbf{E}_i(\mathbf{r})$  and the emission from all other secondary sources. In other words, the target and the random medium build up a self-consistent scattering system.

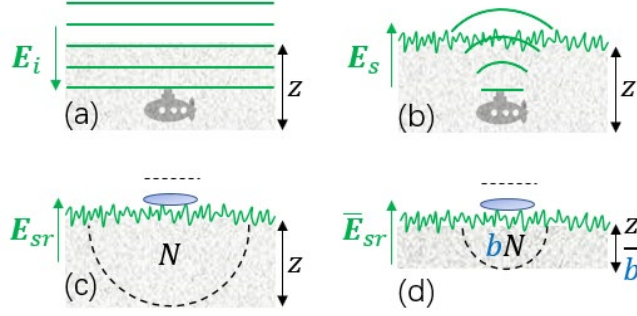


Figure 27: Simplified description of active imaging through a random medium comprising.

(a) an incident plane wave  $\mathbf{E}_i(\mathbf{r})$ , (b) the scattered field  $\mathbf{E}_s(\mathbf{r})$ , and (c) the scattered field emitted from the random medium  $\mathbf{E}_{sr}(\mathbf{r})$ . (d) A statistically equivalent emission  $\bar{\mathbf{E}}_{sr}(\mathbf{r})$  from a scaled down medium.

In many practical situations, one can often consider that only the surface of the target  $S_t$  is contributing to  $\mathbf{E}_{st}(\mathbf{r})$ . In other words, the target is regarded as a surface rather than a volume secondary source. Moreover, the target size is usually much smaller than the thickness  $z$  of the random medium; thus, at points  $\mathbf{r}_e \in S_t \cup V_r$ , the excitation is primarily determined by  $\mathbf{E}_{sr}(\mathbf{r})$ , which means that

$$\mathbf{E}_s(\mathbf{r}_e) \approx k_0^2 \int_{V_r} [m^2(\mathbf{r}') - 1] \vec{G}(\mathbf{r}_e, \mathbf{r}') \cdot [\mathbf{E}_i(\mathbf{r}') + \mathbf{E}_s(\mathbf{r}')] d^3\mathbf{r}'. \quad (12)$$

In this way, the target is excluded from the self-consistent calculation extended over  $V_r$  while both  $\mathbf{E}_i(\mathbf{r})$  and the random medium determine its excitation.

If the particle number density  $N$  is small enough such that any two particles are in the far-field of each other, the independent scattering approximation (ISA) can be applied to estimate transport mean free path  $l^* \approx [N\sigma_{ext}(1-g)]^{-1}$  and optical density  $OD = N\sigma_{ext}z$ , where  $\sigma_{ext}$  is extinction cross-section of a single particle and  $g$  is scattering anisotropy [34].

When the configuration of the scattering medium changes in time, the target is excited, on average, by a “coherent field” that can be approximated as  $\mathbf{E}_{tot}(\mathbf{r} \in S_t) \approx \mathbf{E}_i(\mathbf{r} \in S_t) \exp\left(-\frac{N\sigma_{ext}}{2} \frac{z_t}{\cos(\theta_i)}\right)$  [72]. Here  $z_t$  is the depth of the target and  $\theta_i$  is the angle of incidence. Therefore, the embedded target is equivalent to a secondary source excited by an attenuated  $\mathbf{E}_i(\mathbf{r})$ .

In the next computational step, one must use Eq. (12) to evaluate the excitation of the scattering medium, which enables estimating the vectorial field  $\mathbf{E}_{sr}(\mathbf{r} \in O)$  across the observation plane  $O$ . Since the solution of the Maxwell’s equations is unique for determined boundary conditions, the exact solution of  $\mathbf{E}_{sr}(\mathbf{r} \in O)$  can only be found using the real boundary conditions associated with the practical situation. For realistic imaging scenarios involving a very large number of scattering particles, it is practically impossible to conduct such computation. In the following, we will present an alternative way to achieve an approximate description of  $\mathbf{E}_{sr}(\mathbf{r} \in O)$  which is statistically equivalent to the exact solution.

Let us assume, as suggested in Figure 27(c), that the target is imaged by a system situated at the surface of the random medium. In this case, it is unnecessary to evaluate  $\mathbf{E}_{sr}(\mathbf{r} \in O)$  outside the aperture of the imaging system. Since  $\vec{G}(\mathbf{r}, \mathbf{r}_e)$  is inversely proportional to  $|\mathbf{r} - \mathbf{r}_e|$  [65], the field  $\mathbf{E}_{sr}(\mathbf{r} \in O)$  within the aperture is mainly determined by all the particles inside the hemisphere of radius  $z$  and, therefore, the number of particles necessary for simulating real boundary conditions reduces to  $M = \frac{2}{3}\pi z^3 N$ . As a result, the scattering problem is scaled down as suggested in Figure 27(d). To maintain the overall OD, the density of particles increases to  $bN$  when the thickness scales to  $z/b$ . However, the number of particles necessary to describe this condition decreases by a factor  $b^{-2}$ :

$$M_b = \frac{2}{3}\pi \left(\frac{z}{b}\right)^3 bN = \frac{M}{b^2}. \quad (13)$$

Of course, the scaling factor  $b$  cannot be increased arbitrarily because we want to maintain the far-field condition of particle scattering typical to ISA. At very large packing densities, the field statistics change significantly [34, 35].

Let us examine in detail the case of a plane wave incidence. Let us further set the origin of coordinates in the center of the collecting aperture of the detection system. Each point in the observation plane  $O$  has its own scaled-down hemisphere (virtual medium), and the relative position and depth of the particle  $m$  within the virtual medium are denoted by  $\frac{\Delta r_m}{b}$  and  $\frac{\Delta z_m}{b}$ , respectively. The excitation field reaching the particle  $m$  can be approximated by the ‘‘coherent field’’  $\mathbf{E}_{tot}^{m,i} \left( \mathbf{r} + \frac{\Delta \mathbf{r}_m}{b} \right) \approx \mathbf{E}_i(\mathbf{r} \in O) \exp \left[ j \left( k_0 \hat{\mathbf{n}}_i \cdot \frac{\Delta \mathbf{r}_m}{b} + \phi_i \right) \right] \exp \left[ -\frac{bN\sigma_{ext}}{2} \frac{\Delta z_m}{b \cos(\theta_i)} \right]$ , where  $\hat{\mathbf{n}}_i$  and  $\phi_i$  are the direction and phase of incident plane wave. Since ISA applies after scaling, most particles are still in the far-field with respect to the observation plane. The direction and the polarization of light scattered by a single particle in far-field is described by the amplitude scattering matrix  $\bar{\mathbf{S}}(-\widehat{\Delta \mathbf{r}}_m, \hat{\mathbf{n}}_i)$  [15], where  $\widehat{\Delta \mathbf{r}}_m$  is the unit vector of particle position. Therefore,  $\mathbf{E}_{sr}$  at the observation plane can be estimated as:

$$\mathbf{E}_{sr}(\mathbf{r} \in O) \approx \sum_{m=1}^{M/b^2} \frac{\exp\left(\frac{jk_0|\Delta r_m|}{b}\right)}{|\Delta r_m|/b} \bar{\mathbf{S}}(-\widehat{\Delta \mathbf{r}}_m, \hat{\mathbf{n}}_i) \mathbf{E}_{tot}^{m,i} \left( \mathbf{r} + \frac{\Delta \mathbf{r}_m}{b} \right). \quad (14)$$

This expression can be further simplified by defining the amplitude factor  $A_m(\hat{\mathbf{n}}_i) = \frac{1}{|\Delta r_m|} \exp \left[ -\frac{N\sigma_{ext}\Delta z_m}{2\cos(\theta_i)} \right]$  and the roundtrip phase from observation plane to particle  $m$  as  $\varphi_m(\hat{\mathbf{n}}_i; b) = \frac{k_0}{b} (\hat{\mathbf{n}}_i \cdot \Delta \mathbf{r}_m + |\Delta \mathbf{r}_m|)$ . In these conditions, Eq. (14) becomes:

$$\mathbf{E}_{sr}(\mathbf{r} \in O) \approx b \sum_{m=1}^{M/b^2} \exp[j\varphi_m(\hat{\mathbf{n}}_i; b)] A_m(\hat{\mathbf{n}}_i) \bar{\mathbf{S}}(-\widehat{\Delta \mathbf{r}}_m, \hat{\mathbf{n}}_i) \mathbf{E}_i(\mathbf{r} \in O) \exp(j\phi_i). \quad (15)$$

If for each realization of the random medium the particles are randomly and uniformly distributed, the relative position of the particle  $m$  can be treated statistically as a multivariate random variable. The same statistical treatment extends to all the position-dependent variables in Eq. (15),  $\{\varphi_m(\hat{\mathbf{n}}_i; b), A_m(\hat{\mathbf{n}}_i), \bar{\mathbf{S}}(-\widehat{\Delta\mathbf{r}}_m, \hat{\mathbf{n}}_i)\}$ , to cover the contributions from particles located at any position within the half-space.

Since, in order to maintain ISA, the scaling factor  $b$  cannot be too large,  $\varphi_m(\hat{\mathbf{n}}_i; b)$  will still be fast-varying as a function of particle's position compared to the other components of the multivariate random variable, i.e.  $\{A_m(\hat{\mathbf{n}}_i), \bar{\mathbf{S}}(-\widehat{\Delta\mathbf{r}}_m, \hat{\mathbf{n}}_i)\}$ . In other words,  $p[\varphi_m(\hat{\mathbf{n}}_i; b), A_m(\hat{\mathbf{n}}_i), \bar{\mathbf{S}}(-\widehat{\Delta\mathbf{r}}_m, \hat{\mathbf{n}}_i)]$  can be approximated as  $p_1[\varphi_m(\hat{\mathbf{n}}_i; b)]p_2[A_m(\hat{\mathbf{n}}_i), \bar{\mathbf{S}}(-\widehat{\Delta\mathbf{r}}_m, \hat{\mathbf{n}}_i)]$ . Thus, Eq. (15) can be written as:

$$\mathbf{E}_{sr}(\mathbf{r} \in O) \approx b \sum_{m=1}^{M/b^2} \exp[j\varphi_m(\hat{\mathbf{n}}_i; b)] \mathbf{Y}^{m,i}(\mathbf{r} \in O) \quad (16)$$

where  $\mathbf{Y}^{m,i}(\mathbf{r} \in O)$  represents the net effect from the particle  $m$ , considering the  $\{A_m(\hat{\mathbf{n}}_i), \bar{\mathbf{S}}(-\widehat{\Delta\mathbf{r}}_m, \hat{\mathbf{n}}_i)\}$  and incident light.

Since  $\varphi_m(\hat{\mathbf{n}}_i; b)$  is fast-varying with the particle's position, it can be considered to be an independent, uniformly distributed random variable, i.e.  $p_1(\tilde{\varphi}) = 1/2\pi$ , and Eq. (16) simplifies further as:

$$\mathbf{E}_{sr}(\mathbf{r} \in O) \approx b \sum_{m=1}^{M/b^2} \exp(j\tilde{\varphi}) \mathbf{Y}^{m,i}(\mathbf{r} \in O) \approx b \sum_{m=1}^{M/b^2} \mathbf{Z}^{m,i}(\mathbf{r} \in O), \quad (17)$$

where  $\mathbf{Z}^{m,i}(\mathbf{r} \in O)$  is, in general, a six-element multivariate random variable comprising the real and imaginary parts of field along XYZ. These six elements are pairwise correlated on particle's position, and have zero mean due to fast-varying phase on particle's position. Thus, in comparison to the physical problem described by the superposition of  $M$  random fields, our scaling procedure

introduces only two modifications: a common scaling factor  $b$  and fewer elements  $M/b^2$  in the overall summation.

Since particles continue to be in far-field of each other even after scaling, they are still randomly positioned. In other words,  $\mathbf{Z}^{m,i}(\mathbf{r} \in O)$  contributions from different particles are independent of each other. Thus, for sufficiently large  $M/b^2$ , the multivariate central limit theorem applies to Eq. (17) [136]. It follows that the probability distribution of  $\mathbf{E}_{sr}(\mathbf{r} \in O)$ , the superposition of  $M/b^2$  random vectors, converges to six-dimensional Gaussian  $N_6(0, M\Sigma_m)$ , where the covariance matrix  $\Sigma_m$  describes the correlation between the six elements of  $\mathbf{Z}^{m,i}(\mathbf{r} \in O)$  on particle's position. Therefore, the probability distribution of  $\mathbf{E}_{sr}(\mathbf{r} \in O)$  is not modified by scaling down the random medium.

### 3.2.2 Vector Wave Solution

In the following numerical experiments, all particles are assumed to be spherical; thus, vectorial speckles can be approximated by generalized multi-particle Mie-solution and solved numerically by T-matrix method [137, 138]. When the spatial distribution of spheres resembles an atomic gas, multiple spheres can be randomly packed using, for example, the Lubachevsky-Stillinger algorithm [139, 140].

Following numerical experiments are designed to mimic the conditions for imaging through 1 km fog. The fog is composed of spherical water droplets with diameter  $a$  is  $20 \mu m$ , and density  $N$  is  $10^6/m^3$ . We set the wavelength of incident light  $\lambda=10 \mu m$  since around this value the visibility in fog conditions is known to be reasonably good [62]. The corresponding refractive index for the water droplets is  $1.42-i0.002$ . For illumination, we use a normally incident plane

wave which is linearly polarized along Y direction. For calculations, the amplitude of the electric field is set to be  $1 V/m$ . 2D targets of different shapes are located behind the 1 km fog and we consider that their rough surface have a specular reflectivity limited to  $6 \times 10^{-7}$ . To complete the imaging setup, a thin lens with an aperture diameter of 1 cm and focal length 5 cm is placed at  $1 \lambda$  away from the surface such that evanescent coupling is avoided.

Following the procedure outlined here, we set a scaling factor  $b=2 \times 10^5$  such that the thickness of the scattering medium decreases to  $z=5$  mm, and its number density of droplets increases to  $N=2 \times 10^{11}/m^3$ . In these conditions the averaged distance between particles is  $17.1 \lambda$ , so that ISA still applies. After scaling, the total number of particles within a box ( $5 \times 10 \times 10$  mm) is on the order of  $10^5$ , which is  $4 \times 10^{10}$  times smaller than that in the real scattering setting.

The results of vector field calculations across the aperture plane  $\mathbf{r}_a$  are shown in Figure 28. As can be seen, the electric fields polarized in XYZ directions display very different spatial patterns or, in other words, have different distributions in the wavevector space. This selection of wavevector is typical for transport of polarization through multiple scattering sequences [141, 142] and can be interpreted as a manifestation of accumulated geometric phase [143, 144].

The second-order properties of light can also be estimated based on  $\mathbf{E}_{sr}(\mathbf{r}_a)$ . For instance, one could evaluate the Poynting vector of the scattered field  $\mathbf{S}_{sr}(\mathbf{r}_a) = \frac{1}{2} Re\{\mathbf{E}_{sr}(\mathbf{r}_a) \times \mathbf{H}_{sr}^*(\mathbf{r}_a)\}$  [15]. This requires to find the values of  $\mathbf{E}_{sr}(\mathbf{r}_a)$  and the corresponding magnetic field  $\mathbf{H}_{sr}(\mathbf{r}_a) = \frac{1}{i\omega\mu_0} \nabla \times \mathbf{E}_{sr}(\mathbf{r}_a)$  using two close locations (here separated by  $0.1 \lambda$ ), where  $\omega$  is the temporal frequency of incident light, and  $\mu_0$  is permeability of free space. Figure 28(g) depicts the spatial

variation of the magnitude of scattered Poynting vector  $|\mathcal{S}_{sr}(\mathbf{r}_a)|$  evaluated with a spatial resolution of  $0.1 \lambda$ . An example of the corresponding distribution of directions is shown in Figure 28(h) for a smaller area in the detection plane. Optical vortices of opposite polarity are clearly seen as a typical manifestation of the three-dimensional nature of the field [145].

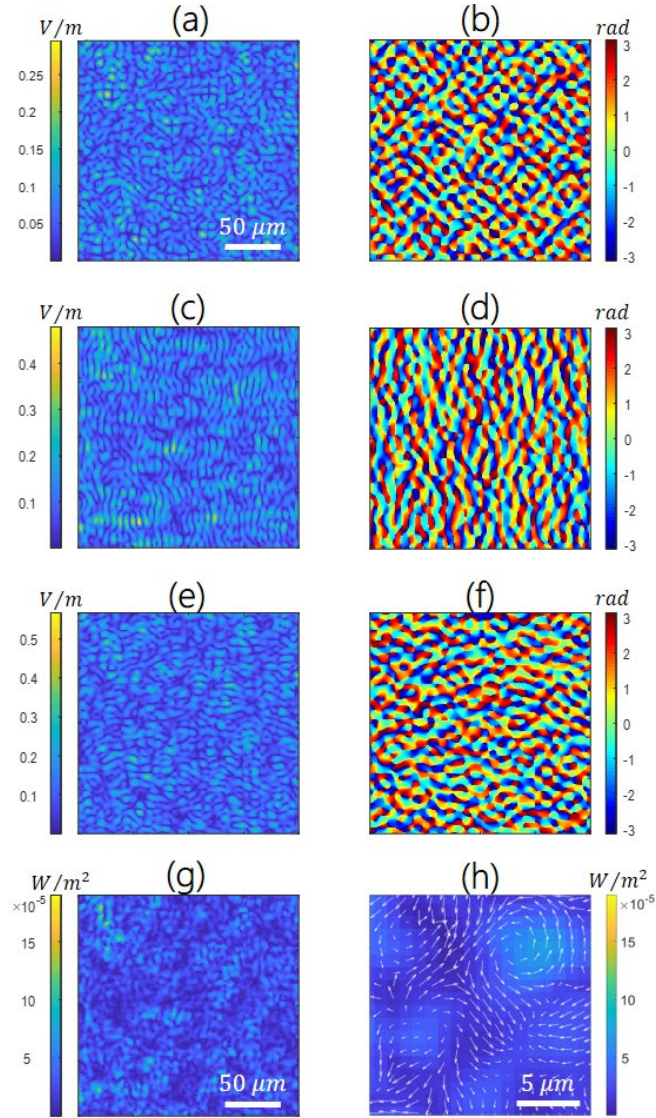


Figure 28: Distribution of random field at the aperture plane.

Amplitude (a) and phase (b) of electric field polarized in X; amplitude (c) and phase (d) of electric field polarized in Y; amplitude (e) and phase (f) of electric field polarized in Z; (g) magnitude of scattered Poynting vector  $|\mathbf{S}_{sr}(\mathbf{r}_a)|$ . (h) The distribution of the scattered Poynting vector  $\mathbf{S}_{sr}(\mathbf{r}_a)$  over a smaller area.

We will now use these results to simulate a realistic imaging outcome where, close to the back focal plane of the thin lens  $\mathbf{r}_f$ , one practically detects the far-field diffraction pattern of

$E_s(\mathbf{r}_a)$  [110]. In other words, the detected field  $E_s(\mathbf{r}_f)$  is essentially transverse [15]. Another critical aspect of a realistic imaging scenario is the fact that the fog “configuration” changes during the measurement. When the exposure time  $\tau_d$  of the detector is shorter than the fog’s characteristic time  $\tau_c$ , the scattering medium can be regarded as static and the measurement is only determined by one spatial realization of the fog. In this case, the scattered wave generates speckles at the imaging plane, as shown in Figure 29(a-e). Notably, in the orthogonal channel,  $E_{s\perp}(\mathbf{r}_f)$  has a spatially stationary distribution of phase while the amplitude displays the so-called Maltese-cross shape due to the corresponding geometric phase. In the parallel channel, the target features are barely distinguishable in the amplitude distribution  $E_{s\parallel}(\mathbf{r}_f)$ . Interestingly, the phase distribution in this case is spatially non-stationary indicating somewhat the presence of the reflective targets.

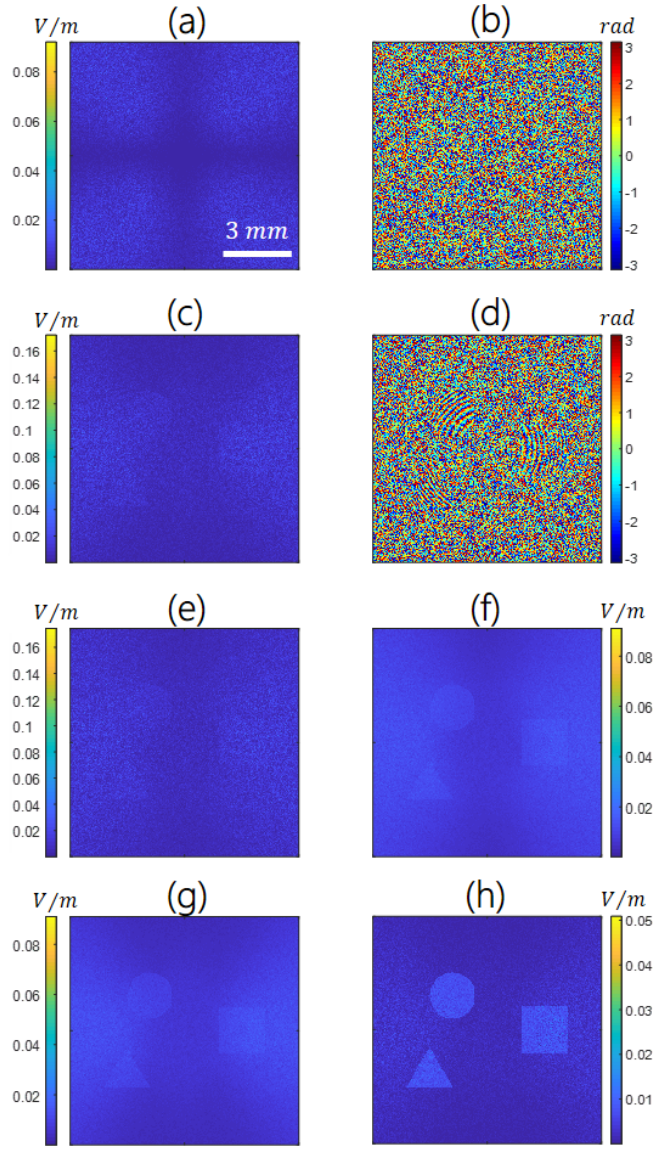


Figure 29: Measurements corresponding to one realization of the random medium.

(a) amplitude and (b) phase of  $E_{s\perp}(\mathbf{r}_f)$ ; amplitude (c) and phase (d) of  $E_{s\parallel}(\mathbf{r}_f)$ ; (e) distribution of field magnitude  $|E_s(\mathbf{r}_f)|$ . Averages over fifteen independent realizations of the random medium: (f) incoherent averaging  $\langle |E_s(\mathbf{r}_f)| \rangle_i$ , (g) polarized incoherent averaging  $\langle |E_{s\parallel}(\mathbf{r}_f)| \rangle_i$ , (h) polarized coherent averaging  $\langle |E_{s\parallel}(\mathbf{r}_f)| \rangle_i$ .

Depending on the measurement procedure, there are also other ways to acquire and process the information. For instance, if the exposure time is much longer,  $\tau_d \gg \tau_c$ , one essentially records an incoherent average over many realizations of the scattering medium. This condition is illustrated in Figure 29(f) where 15 realizations of the scattering medium are averaged leading to better target visibility, albeit with a very poor contrast. The target contrast is only slightly improved by adding a linear polarizer in front of the detector as shown in Figure 29(g) where the contribution of  $E_{s\perp}(\mathbf{r}_f)$  is suppressed from the calculation.

However, if field can be measured sufficiently fast such that  $\tau_d < \tau_c$  and many realizations can be recorded, a coherent processing is possible [64]. As shown in Figure 29(h), the contrast and the resolution improve significantly and, after averaging  $E_{s\parallel}(\mathbf{r}_f)$  for 15 times, the edges of targets are obvious. Since the re-emission of light from random media can be regarded as “coherent noise”, each realization of  $\mathbf{E}_{sr}(\mathbf{r}_f)$  is independent and shares the same probability distribution. A more efficient suppression of “coherent noise” is achieved by averaging on the complex field rather than on the scalar amplitude. Aside from the issue of coherent noise, the ambiguity between targets’ reflectivity and optical depth is also alleviated when the backpropagation procedure relies on field measurements [61, 110].

### 3.2.3 Computational Capabilities

By invoking the linearity of the scattering process, Eq. (16) can be generalized to an arbitrary incident wavefront. For any particle  $m$ , the roundtrip phases  $\varphi_m(\hat{\mathbf{n}}_i; b)$  corresponding to different incident plane waves  $\hat{\mathbf{n}}_i$  are strongly correlated. In other words, Eq. (16) can be regarded as a summation of correlated random variables, which eventually leads to a non-Gaussian field

distribution. Since the origin of any non-Gaussian distribution is problem-specific [146], a particular solution can be found only within the frame of generalized central limit theorems [147]. Finding solutions for a particular example of structured incident field is beyond the scope of this paper.

This scaling method we described provides a statistically equivalent solution under plane wave illumination and reduces the number of necessary particles, especially in the case of large distances  $z$ , which is relevant for most remote sensing scenarios. The simulation presented here was operated on consumer hardware (GeForce GTX 1080 Ti, 64 GB RAM) for 10 hours to simulate one spatial realization of the random medium. Expanding calculations beyond  $10^5$  particles should be technically possible and, therefore, evaluating the imaging performance through larger optical densities should be within reach. Aside from direct imaging applications, this numerical solution for the field distribution can be directly applied to correlation-based modalities such as blind ghost imaging [148].

There are several constraints when scaling down a computational problem involving imaging through random media. Firstly, to avoid significant errors in assessing the magnitude of local excitation fields, the host medium cannot be highly absorbing. Secondly, imaging modalities based on speckle illumination [149] cannot be approached in this way since the target excitation cannot be simply described as a ‘coherent field’. Finally, imaging modalities such as wavefront shaping [150] rely on the actual boundary conditions, which precludes the use of scaled down versions of the kind discussed in this paper

## CHAPTER FOUR: CONCLUSION

We will now summarize the conclusions of our communication for unresolved imaging, which are listed sequentially from subwavelength information to multiple scattering.

Phase is a common wave parameter used to describe the consequences of light–matter interaction. When the scattering center is smaller than the wavelength, a simplistic geometric interpretation of the measured phase is insufficient. Using energetic arguments, we show that the appropriate description of measurements performed far away from subwavelength objects involves the duration and the effective volume of the elastic scattering event. Because the evanescent fields contribute significantly to coupling and releasing of energy, the effective interaction volume is significantly larger than the physical size of subwavelength particles. Our results also provide means to describe scattering phenomena in dense media where scatterers are in close proximity to each other. One potential future direction is to investigate the energetic description of subwavelength scattering with anisotropic polarizabilities.

To quantitatively measure the tiny phase in subwavelength scattering, I demonstrate that polarization encoding provides a convenient way to realize a robust common-path interferometer for measuring both the phase and the amplitude of scattered optical fields. Moreover, for a given detector array, the design allows maximizing the interferometric visibility and, therefore, permits reaching the sensitivity limit for the field measurement. The approach is of particular interest for inefficient scattering scenarios such as subwavelength scattering. One potential future direction is to optimize the engineering parts of this system, so it can function as an add-on module to commercial microscopes.

For mitigating multiple scattering, we developed a new Monte Carlo method for calculating the propagation of a two-point optical property, namely the spatial coherence function. Here we considered only scalar problem, however our method can be extended for calculation of full polarization-coherence matrix as Monte Carlo allows simple generalization to the vector case [151]. Our method is based on the Wigner transformation that converts the angular distribution of propagating ‘photons’ into local, coherent field properties. As the angular distribution of ‘photons’ is vital for the good performance of our method, the rigorous Mie scattering phase functions were used for Monte Carlo simulations instead of conventional Henyey-Greenstein approximation. Test calculations were performed for spatial coherence function in both transmission and reflection from plane-parallel slabs of inhomogeneous scattering media with different optical thicknesses. Finally, the SCF transformation was studied here in plane-parallel geometries, but our Monte Carlo calculations can be used without any modification to treat scattering media with arbitrary complex shapes as opposed to other numerical methods such as discrete ordinates [104].

This new Monte Carlo method can be applied to non-line-of-sight scenarios. Traditional optical imaging requires either straight-line access to the object or a specific arrangement of specular reflectors that create a wrapped version of unobstructed imaging. Non-line-of-sight sensing can also be achieved but only by purposely controlling some of the properties of light during the measurement process. In the previous sections, we have shown that information about a non-line-of-sight object can be obtained completely passively without using mirrors and without any access to the source of natural light. For this, we exploit a higher-dimensionality degree of freedom of the optical field. We have shown that the spatial coherence properties of light are not completely destroyed upon reflection from a scattering medium especially for shears perpendicular

to the plane of incidence (‘glitter path’ effect). Moreover, the effect of incoherent volume scattering can be effectively suppressed in practice by limiting the field-of-view of the detection instrument. This proves that, in certain conditions of incidence, a diffuse reflector can act as a “broken mirror” for the complex coherence function of light, which can still permit recovering relevant spatial information about the object.

Multiple scattering can also be mitigated coherently, and previous sections provide a statistically-equivalent, scaled model for active imaging through random media. When a target is embedded in random media, the quality of optical imaging can be improved by actively controlling the illumination and exploiting vector wave properties. A rigorous description, however, requires expensive computational resources to fully account for the electromagnetic boundary conditions. Here, we introduce a statistically equivalent scaling model that allows for reducing the complexity of the problem. The new scheme describes the entanglement between the local wave vector and the polarization state in random media and also accounts for cumulative properties such as geometric phase. The approach is validated for different scenarios where the coherent background noise alters substantially the performance of active imaging. One potential future direction is to explore specific beams other than plane waves.

## LIST OF PUBLICATIONS

- 1 Z. Shen, and A. Dogariu, “Vector wave simulation of active imaging through random media,” *JOSA A* 37(6), 908-913 (2020).
- 2 Z. Shen, S. Cui, and A. Dogariu, “Polarization-encoded field measurement in subwavelength scattering,” *Opt. Lett.* 44(14), 3446-3449 (2019).
- 3 Z. Shen, and A. Dogariu, “Meaning of phase in subwavelength elastic scattering,” *Optica* 6(4), 455-459 (2019).
- 4 M. Batarseh, S. Sukhov, Z. Shen, H. Gemar, R. Rezvani, and A. Dogariu, “Passive sensing around the corner using spatial coherence,” *Nat. Commun.* 9, 1-6 (2018).
- 5 Z. Shen, S. Sukhov, and A. Dogariu, “Monte Carlo method to model optical coherence propagation in random media,” *JOSA A* 34, 2189–2193 (2017).

## LIST OF REFERENCES

- 1 B. E. Saleh, and M. C. Teich, *Fundamentals of photonics* (John Wiley & Sons, 2019).
- 2 J. Jonkman, C. M. Brown, G. D. Wright, K. I. Anderson, and A. J. North, “Tutorial: guidance for quantitative confocal microscopy,” *Nat. Protoc.* 1-27 (2020).
- 3 S. J. Sahl, S. W. Hell, and S. Jakobs, “Fluorescence nanoscopy in cell biology,” *Nat. Rev. Mol.* 18(11), 685 (2017).
- 4 J. G. Carlton, H. Jones, and U. S. Eggert, “Membrane and organelle dynamics during cell division,” *Nat. Rev. Mol.* 1-16 (2020).
- 5 R. L. Huston, “On centrioles, microtubules, and cellular electromagnetism,” *Journal of Nanotechnology in Engineering and Medicine* 5(3) (2014).
- 6 M. Fernández-Suárez, and A. Y. Ting, “Fluorescent probes for super-resolution imaging in living cells,” *Nat. Rev. Mol.* 9(12), 929-943 (2008).
- 7 Z. Shen, S. Cui, and A. Dogariu, “Polarization-encoded field measurement in subwavelength scattering,” *Opt. Lett.* 44(14), 3446-3449 (2019).
- 8 Y. Altmann, S. McLaughlin, M. J. Padgett, V. K. Goyal, A. O. Hero, and D. Faccio, “Quantum-inspired computational imaging,” *Science* 361(6403) (2018).
- 9 A. Beckus, A. Tamasan, and G. K. Atia, “Multi-modal non-line-of-sight passive imaging,” *IEEE Transactions on Image Processing* 28(7), 3372-3382 (2019).
- 10 A. Beckus, A. Tamasan, A. Dogariu, A. F. Abouraddy, G. K. Atia, “On the inverse problem of source reconstruction from coherence measurements,” *JOSA A* 35(6), 959-968 (2018).

- 11 Z. Shen, and A. Dogariu, "Vector wave simulation of active imaging through random media," *JOSA A* 37(6), 908-913 (2020).
- 12 A. Sommerfeld, *Optics. Lectures on Theoretical Physics, Vol. IV*, (Academic Press, New York, 1964).
- 13 M. Born and E. Wolf, *Principles of Optics*, (Cambridge University Press, Cambridge, 1999).
- 14 N. B. Sawyer, S. P. Morgan, M. G. Somekh, C. W. See, E. Astrakharchik-Farrimond, and B. Y. Shekunov, "Amplitude and phase microscopy for sizing of spherical particles," *Appl. Opt.* 42(22), 4488-4498 (2003).
- 15 C. F. Bohren, and D. R. Huffman, *Absorption and scattering of light by small particles* (John Wiley & Sons, 2008).
- 16 J. R. Fienup, "Phase retrieval algorithms: a comparison," *Appl. Opt.* 21(15), 2758-2769 (1982).
- 17 G. Popescu, T. Ikeda, R. R. Dasari, and M. S. Feld, "Diffraction phase microscopy for quantifying cell structure and dynamics," *Opt. Lett.* 31(6), 775-777 (2006).
- 18 D. Murphy, R. Oldfield, S. Schwartz, and M. Davidson, "Introduction to Phase Contrast Microscopy," <https://www.microscopyu.com/techniques/phase-contrast/introduction-to-phase-contrast-microscopy>
- 19 Z. Shen, and A. Dogariu, "Meaning of phase in subwavelength elastic scattering," *Optica* 6(4), 455-459 (2019).
- 20 E. P. Wigner, "Lower limit for the energy derivative of the scattering phase shift," *Phys. Rev.* 98(1), 145 (1955).
- 21 C. A. de Carvalho, and H. M. Nussenzveig, "Time delay," *Phys. Rep.* 364(2), 83-174 (2002).

- 22 H. G. Winful, "Tunneling time, the Hartman effect, and superluminality: A proposed resolution of an old paradox," *Phys. Rep.* 436(1-2), 1-69 (2006).
- 23 B. T. Draine, and P. J. Flatau, "Discrete-dipole approximation for scattering calculations," *JOSA A* 11(4), 1491-1499 (1994).
- 24 R. Carminati, J. J. Greffet, C. Henkel, and J. M. Vigoureux, "Radiative and non-radiative decay of a single molecule close to a metallic nanoparticle," *Opt. Commun.* 261(2), 368-375 (2006).
- 25 D. N. Pattanayak, and E. Wolf. "General form and a new interpretation of the Ewald-Oseen extinction theorem," *Opt. Commun.* 6(3), 217-220 (1972).
- 26 F. T. Smith, "Lifetime matrix in collision theory," *Phys. Rev.* 118(1), 349 (1960).
- 27 S. Rotter, and S. Gigan, "Light fields in complex media: Mesoscopic scattering meets wave control," *Rev. Mod. Phys.* 89(1), 015005 (2017).
- 28 M. I. Mishchenko, and L. D. Travis, "Gustav Mie and the evolving discipline of electromagnetic scattering by particles," *Bulletin of the American Meteorological Society* 89(12), 1853-1862 (2008).
- 29 A. Lagendijk, and B. A. Van Tiggelen, "Resonant multiple scattering of light," *Phys. Rep.* 270(3), 143-215 (1996).
- 30 J. Schäfer, S. C. Lee, and A. Kienle, "Calculation of the near fields for the scattering of electromagnetic waves by multiple infinite cylinders at perpendicular incidence," *J. Quant. Spectrosc. Radiat. Transf.* 113(16), 2113-2123 (2012).
- 31 J. Schäfer, "MatScat", <https://www.mathworks.com/matlabcentral/fileexchange/36831-matscat>

- 32 A. Bott, and W. Zdunkowski, "Electromagnetic energy within dielectric spheres," *JOSA A* 4(8), 1361-1365 (1987).
- 33 M. Potenza and P. Milani, "Free nanoparticle characterization by optical scattered field analysis: opportunities and perspectives", *J. Nanopart. Res.* 16(2680) (2014).
- 34 R. Rezvani Naraghi, S. Sukhov, J. J. Saenz, and A. Dogariu, "Near-field effects in mesoscopic light transport," *Phys. Rev. Lett.* 115, 203903 (2015).
- 35 R. Rezvani Naraghi and A. Dogariu, "Phase transitions in diffusion of light," *Phys. Rev. Lett.* 117, 263901 (2016).
- 36 P. M. Saulnier, M. P. Zinkin, and G. H. Watson, "Scatterer correlation effects on photon transport in dense random media," *Phys. Rev. B* 42(4), 2621 (1990).
- 37 A. Ishimaru and Y. Kuga, "Attenuation constant of a coherent field in a dense distribution of particles," *JOSA* 72(10), 1317-1320 (1982).
- 38 R. Shinde, G. Balgi, S. Richter, S. Banerjee, J. Reynolds, J. Pierce and E. Sevick-Muraca, "Investigation of static structure factor in dense suspensions by use of multiply scattered light," *Appl. Opt.* 38(1), 197-204 (1999).
- 39 R. West, D. Gibbs, L. Tsang and A. K. Fung, "Comparison of optical scattering experiments and the quasi-crystalline approximation for dense media," *JOSA A* 11(6), 1854-1858 (1994).
- 40 D. N. Pattanayak, and E. Wolf. "General form and a new interpretation of the Ewald-Oseen extinction theorem," *Opt. Commun.* 6(3), 217-220 (1972).
- 41 P. C. Waterman, "Matrix formulation of electromagnetic scattering," *Proc. IEEE* 53(8), 805-812 (1965).

- 42 M. I. Mishchenko, L. D. Travis, and D. W. Mackowski, "T-matrix computations of light scattering by nonspherical particles: a review," *J. Quant. Spectrosc. Radiat. Transf.* 55(5), 535-575 (1996).
- 43 G. S. Agarwal, "Relation between Waterman's extended boundary condition and the generalized extinction theorem," *Phys. Rev. D* 14(4), 1168 (1976).
- 44 S. Pancharatnam, "Generalized theory of interference and its applications," *Proc. Indian Acad. Sci. A* 44(6), 398-417 (1956).
- 45 K. Creath, "Phase-measurement interferometry techniques," *Prog. Optics* 26(26), 349-393 (1988).
- 46 P. Hosseini, R. Zhou, Y. H. Kim, C. Peres, A. Diaspro, C. Kuang, Z. Yaqoob, and P. T. So, "Pushing phase and amplitude sensitivity limits in interferometric microscopy," *Opt. Lett.* 41(7), 1656-1659 (2016).
- 47 J. Ortega-Arroyo, and P. Kukura, "Interferometric scattering microscopy (iSCAT): new frontiers in ultrafast and ultrasensitive optical microscopy," *Phys. Chem. Chem. Phys.* 14(45), 15625-15636 (2012).
- 48 B. O. Leung, and K. C. Chou, "Review of super-resolution fluorescence microscopy for biology," *Appl. Spectrosc.* 65(9), 967-980 (2011).
- 49 U. Kubitscheck, O. Kückmann, T. Kues, and R. Peters, "Imaging and tracking of single GFP molecules in solution," *Biophys. J.* 78(4), 2170-2179 (2000).
- 50 R. E. Thompson, D. R. Larson, and W. W. Webb, "Precise nanometer localization analysis for individual fluorescent probes," *Biophys. J.* 82(5), 2775-2783 (2002).

- 51 R. J. Ober, S. Ram, and E. S. Ward, “Localization accuracy in single-molecule microscopy,” *Biophys. J.* 86(2), 1185-1200 (2004).
- 52 G. E. Snyder, T. Sakamoto, J. A. Hammer III, J. R. Sellers, and P. R. Selvin, “Nanometer localization of single green fluorescent proteins: evidence that myosin V walks hand-over-hand via telemark configuration,” *Biophys. J.* 87(3), 1776-1783 (2004).
- 53 Z. Wang, L. Millet, M. Mir, H. Ding, S. Unarunotai, J. Rogers, ... and G. Popescu, “Spatial light interference microscopy (SLIM),” *Opt. Express* 19(2), 1016-1026 (2011).
- 54 G. Young, N. Hundt, D. Cole, A. Fineberg, J. Andrecka, A. Tyler, ... and P. Kukura, “Quantitative mass imaging of single biological macromolecules,” *Science* 360(6387), 423-427 (2018).
- 55 D. Cole, G. Young, A. Weigel, A. Sebesta, and P. Kukura, “Label-free single-molecule imaging with numerical-aperture-shaped interferometric scattering microscopy,” *ACS Photonics* 4(2), 211-216 (2017).
- 56 M. Liebel, J. T. Hugall, and N. F. van Hulst, “Ultrasensitive label-free nanosensing and high-speed tracking of single proteins,” *Nano Lett.* 17(2), 1277-1281 (2017).
- 57 Goodman, *Introduction to Fourier Optics* (Roberts and Company Publishers, Englewood, 2005).
- 58 R. K. Tyson, *Principles of Adaptive Optics* (CRC Press, 2015).
- 59 T. Treibitz and Y. Y. Schechner, “Polarization: beneficial for visibility enhancement?” in *IEEE Conference on Computer Vision and Pattern Recognition (CVPR)* (2009).
- 60 K. He, J. Sun, and X. Tang, “Single image haze removal using dark channel prior,” *IEEE Trans. Pattern Anal. Mach. Intell.* 33, 2341–2353 (2011).

- 61 S. G. Narasimhan and S. K. Nayar, “Contrast restoration of weather degraded images,” *IEEE Trans. Pattern Anal. Mach. Intell.* 25, 713–724 (2003).
- 62 J. Viitanen, P. Pyykönen, and R. Täppinen, “Active infrared illumination in fog for driver assistance,” in *10th International Conference on Intelligent Computer Communication and Processing* (2014), pp. 215–218.
- 63 J. S. Jaffe, “Computer modeling and the design of optimal underwater imaging systems,” *IEEE J. Ocean. Eng.* 15, 101–111 (1990).
- 64 A. V. Kanaev, A. T. Watnik, D. F. Gardner, C. Metzler, K. P. Judd, P. Lebow, K. M. Novak, and J. R. Lindle, “Imaging through extreme scattering in extended dynamic media,” *Opt. Lett.* 43, 3088–3091 (2018).
- 65 M. I. Mishchenko, V. P. Tishkovets, L. D. Travis, B. Cairns, J. M. Dlugach, L. Liu, V. K. Rosenbush, and N. N. Kiselev, “Electromagnetic scattering by a morphologically complex object: fundamental concepts and common misconceptions,” *J. Quant. Spectrosc. Radiat. Transfer* 112, 671–692 (2011).
- 66 J. W. Goodman, “Some fundamental properties of speckle,” *J. Opt. Soc. Am.* 66, 1145–1150 (1976).
- 67 S. Chandrasekhar, *Radiative Transfer* (Courier Corporation, 2013).
- 68 Z. Shen, S. Sukhov, and A. Dogariu, “Monte Carlo method to model optical coherence propagation in random media,” *JOSA A* 34, 2189–2193 (2017).
- 69 M. Batarseh, S. Sukhov, Z. Shen, H. Gemar, R. Rezvani, and A. Dogariu, “Passive sensing around the corner using spatial coherence,” *Nat. Commun.* 9, 1-6 (2018).

- 70 A. A. Lacis, J. Chowdhary, M. I. Mishchenko, and B. Cairns, “Modeling errors in diffuse-sky radiation: vector vs scalar treatment,” *Geophys. Res. Lett.* 25, 135–138 (1998).
- 71 M. I. Mishchenko and J. M. Dlugach, “Accuracy of the scalar approximation in computations of diffuse and coherent backscattering by discrete random media,” *Phys. Rev. A* 78, 063822 (2008).
- 72 M. I. Mishchenko, “Vector radiative transfer equation for arbitrarily shaped and arbitrarily oriented particles: a microphysical derivation from statistical electromagnetics,” *Appl. Opt.* 41, 7114–7134 (2002).
- 73 J. M. Schmitt, S. H. Xiang, and K. M. Yung, “Speckle in optical coherence tomography,” *J. Biomed. Opt.* 4, 95–106 (1999).
- 74 E. Akkermans, P. E. Wolf, R. Maynard, and G. Maret, “Theoretical study of the coherent backscattering of light by disordered media,” *J. Phys.* 49, 77–98 (1988).
- 75 L. C. Andrews and R. L. Phillips, *Laser Beam Propagation through Random Media* (SPIE, 1998).
- 76 S. Gigan, “Viewpoint: Endoscopy Slims Down,” *Physics* 5, 127 (2012).
- 77 M. D. Birowosuto, S. E. Skipetrov, W. L. Vos, and A. P. Mosk, “Observation of Spatial Fluctuations of the Local Density of States in Random Photonic Media,” *Phys. Rev. Lett.* 105, 013904 (2010).
- 78 A. Schreiber, K. N. Cassemiro, V. Potoček, A. Gábris, I. Jex, and C. Silberhorn, “Decoherence and Disorder in Quantum Walks: From Ballistic Spread to Localization,” *Phys. Rev. Lett.* 106, 180403 (2011).

- 79 E. Akkermans, G. Montambaux, *Mesoscopic Physics of Electrons and Photons* (Cambridge, UK: Cambridge University Press, 2011).
- 80 F. Martelli, *Light propagation through biological tissue and other diffusive media: theory, solutions, and software* (SPIE, 2010).
- 81 A. Isimaru, *Wave propagation and scattering in random media*. Vol. 1 (New York: Academic press, 1978).
- 82 M. I. Mishchenko, "Calculation of the amplitude matrix for a nonspherical particle in a fixed orientation," *Appl. Opt.* 39, 1026-1031 (2000).
- 83 B. Saleh, *Introduction to subsurface imaging* (Cambridge University Press, 2011).
- 84 S. Sukhov, D. Haefner, A. Dogariu, "Coupled dipole method for modeling optical properties of large-scale random media," *Phys. Rev. E*, 77, 066709 (2008).
- 85 L. Wang, S. L. Jacques, and L. Zheng, "MCML-Monte Carlo modeling of light transport in multi-layered tissues," *Comput. Methods Programs Biomed.* 47, 131–146 (1995).
- 86 S. Bartel and A. H. Hielscher, "Monte Carlo simulations of the diffuse backscattering Mueller matrix for highly scattering media," *Appl. Opt.* 39, 1580–1588 (2000).
- 87 M. Xu, "Electric field Monte Carlo simulation of polarized light propagation in turbid media," *Opt. Express* 26, 6530–6539 (2004).
- 88 J. C. Ramella-Roman, S. A. Prahl, and S. L. Jacques, "Three Monte Carlo programs of polarized light transport into scattering media: part I," *Opt. Express* 13, 4420–4438 (2005).

- 89 J. C. Ramella-Roman, S. A. Prah1, and S. L. Jacques, "Three Monte Carlo programs of polarized light transport into scattering media: part II," *Opt. Express* 13, 10392–10405 (2005).
- 90 J. W. Goodman, *Statistical optics* (New York: John Wiley & Sons, 2015).
- 91 G. Yao and L. V. Wang, "Monte Carlo simulation of an optical coherence tomography signal in homogeneous turbid media," *Phys. Med. Biol.* 44, 2307–2320 (1999).
- 92 Q. Lu, X. Gan, M. Gu, and Q. Luo, "Monte Carlo modeling of optical coherence tomography imaging through turbid media," *Appl. Opt.* 43, 1628–1637 (2004).
- 93 A. Prodi, E. Knudsen, P. Willendrup, S. Schmitt, C. Ferrero, R. Feidenhans'l, and K. Lefmann, "A Monte Carlo approach for simulating the propagation of partially coherent x-ray beams," *Proc. SPIE* 8141, 814108 (2011).
- 94 V. A. Borovikov and B. E. Kinber, *Geometrical Theory of Diffraction*, IEEE Electromagnetic Wave Series 37 (IET, 1994).
- 95 V. R. Daria, C. Saloma, and S. Kawata, "Excitation with a focused, pulsed optical beam in scattering media: diffraction effects," *Appl. Opt.* 39, 5244–5255 (2000).
- 96 D. G. Fischer, S. A. Prah1, and D. D. Duncan, "Monte Carlo modeling of spatial coherence: free-space diffraction," *JOSA A* 25, 2571-2581 (2008).
- 97 S. A. Prah1, D. D. Duncan, D. G. Fischer, "Stochastic Huygens and Partial Coherence Propagation through Thin Tissues," *Proc. of SPIE* 7573, 75730D (2010).
- 98 C. Mujat and A. Dogariu, "Statistics of partially coherent beams: a numerical analysis," *JOSA A* 21, 1000-1003 (2004).

- 99 A. Tycho and T. M. Jørgensen, Comment on “Excitation with a focused, pulsed optical beam in scattering media: diffraction effects,” *Appl. Opt.* 41, 4709–4711 (2002).
- 100 S. Moon, D. Kim, and E. Sim, “Monte Carlo study of coherent diffuse photon transport in a homogeneous turbid medium: a degree-of-coherence based approach,” *Appl. Opt.* 47, 336-345 (2008).
- 101 M. Kraszewski, M. Trojanowski, M. R. Strijkowski and J. Pluciński, “Simulating the coherent light propagation in a random scattering materials using the perturbation expansion”, *Proc. of SPIE* 9526, 95260M (2015).
- 102 M.j Kraszewski and J. Pluciński, “Coherent Wave Monte Carlo method for simulating light propagation in tissue,” *Proc. of SPIE* 9706, 970611 (2016).
- 103 S. John, G. Pang, and Y. Yang, “Optical coherence propagation and imaging in a multiple scattering medium,” *J. Biomed. Opt.* 1, 180–191 (1996).
- 104 R. Pierrat, J.-J. Greffet, and R. Carminati, R. Elaloufi, “Spatial coherence in strongly scattering media,” *JOSA A* 22, 2329-2337 (2005).
- 105 E. Wolf, “Coherence and radiometry,” *JOSA* 68(1), 6-17 (1978).
- 106 C.-C. Cheng and M. G. Raymer, “Propagation of transverse optical coherence in random multiple-scattering media,” *Phys. Rev. A* 62, 023811 (2000).
- 107 E. Baleine and A. Dogariu, "Propagation of partially coherent beams through particulate media," *JOSA A* 20, 2041-2045 (2003).
- 108 D. Toubienc, “Henyey–Greenstein and Mie phase functions in Monte Carlo radiative transfer computations,” *Appl. Opt.* 35, 3270-3274 (1996).

- 109 P. Naglič, F. Pernuš, B. Likar, and M. Bürmen, “Lookup table-based sampling of the phase function for Monte Carlo simulations of light propagation in turbid media,” *Biomed. Opt. Express* 8, 1895-1910 (2017).
- 110 Goodman, *Introduction to Fourier Optics* (Roberts and Company Publishers, Englewood, 2005).
- 111 J. N. Mait, G. W. Euliss, and R. A. Athale, “Computational imaging,” *Adv. Opt. Photonics* 10, 409–483 (2018).
- 112 I. M. Vellekoop, and A. Mosk, “Focusing coherent light through opaque strongly scattering media,” *Opt. Lett.* 32, 2309–2311 (2007).
- 113 S. Popoff, G. Lerosey, M. Fink, A. C. Boccara, and S. Gigan, “Image transmission through an opaque material,” *Nat. Commun.* 1, 81 (2010).
- 114 T. Kohlgraf-Owens, and A. Dogariu, “Finding the field transfer matrix of scattering media,” *Opt. Express* 16, 13225–13232 (2008).
- 115 S. M. Popoff, G. Lerosey, R. Carminati, M. Fink, A. C. Boccara, and S. Gigan, “Measuring the transmission matrix in optics: an approach to the study and control of light propagation in disordered media,” *Phys. Rev. Lett.* 104, 100601 (2010).
- 116 H. He, Y. Guan, and J. Zhou, “Image restoration through thin turbid layers by correlation with a known object,” *Opt. Express* 21, 12539–12545 (2013).
- 117 X. Xu, H. Liu, and L. V. Wang, “Time-reversed ultrasonically encoded optical focusing into scattering media,” *Nat. Photonics* 5, 154–157 (2011).

- 118 A. Velten, T. Willwacher, O. Gupta, A. Veeraraghavan, M. G. Bawendi, and R. Raskar, “Recovering three-dimensional shape around a corner using ultrafast time-of-flight imaging,” *Nat. Commun.* 3, 745 (2012).
- 119 M. O’Toole, D. B. Lindell, and G. Wetzstein, “Confocal non-line-of-sight imaging based on the light-cone transform,” *Nature* 555, 338 (2018).
- 120 X. Xu, X. Xie, H. He, H. Zhuang, J. Zhou, A. Thendiyammal, and A. P. Mosk, “Imaging objects through scattering layers and around corners by retrieval of the scattered point spread function,” *Opt. Express* 25, 32829–32840 (2017).
- 121 O. Katz, E. Small, and Y. Silberberg, “Looking around corners and through thin turbid layers in real time with scattered incoherent light,” *Nat. Photonics* 6, 549–553 (2012).
- 122 O. Katz, P. Heidmann, M. Fink, and S. Gigan, “Non-invasive single-shot imaging through scattering layers and around corners via speckle correlations,” *Nat. Photonics* 8, 784–790 (2014).
- 123 E. Edrei, and G. Scarcelli, “Optical imaging through dynamic turbid media using the Fourier-domain shower-curtain effect,” *Optica* 3, 71–74 (2016).
- 124 A. K. Singh, D. N. Naik, G. Pedrini, M. Takeda, and W. Osten, “Looking through a diffuser and around an opaque surface: a holographic approach,” *Opt. Express* 22, 7694–7701 (2014).
- 125 J. Klein, C. Peters, J. Martín, M. Laurenzis, and M. B. Hullin, “Tracking objects outside the line of sight using 2D intensity images,” *Sci. Rep.* 6, 32491 (2016).
- 126 G. Gariepy, F. Tonolini, R. Henderson, J. Leach, and D. Faccio, “Detection and tracking of moving objects hidden from view,” *Nat. Photonics* 10, 23–26 (2016).

- 127 A. Beckus, A. Tamasan, A. Dogariu, A. F. Abouraddy, and G. K. Atia, “Spatial coherence of fields from generalized sources in the Fresnel regime,” *JOSA A* 34, 2213–2221 (2017).
- 128 W. Wang, R. Simon, and E. Wolf, “Changes in the coherence and spectral properties of partially coherent light reflected from a dielectric slab,” *JOSA A* 9, 287–297 (1992).
- 129 C.-C. Cheng, and M. Raymer, “Long-range saturation of spatial decoherence in wave-field transport in random multiple-scattering media,” *Phys. Rev. Lett.* 82, 4807 (1999).
- 130 Y. Sun, “Statistical ray method for deriving reflection models of rough surfaces,” *JOSA A* 24, 724–744 (2007).
- 131 J. Ogilvy, “Wave scattering from rough surfaces,” *Rep. Progress. Phys.* 50, 1553–1608 (1987).
- 132 B. Smith, “Geometrical shadowing of a random rough surface,” *IEEE Trans. Antennas Propag.* 15, 668–671 (1967).
- 133 J. A. Adam, *A Mathematical Nature Walk*, Vol. 137 (Princeton University Press, Princeton, NJ, 2011).
- 134 D. K. Lynch, D. S. Dearborn, and J. A. Lock, “Glitter and glints on water,” *Appl. Opt.* 50, F39–F49 (2011).
- 135 R. R. Naraghi, H. Gemar, M. Batarseh, A. Beckus, G. Atia, S. Sukhov, and A. Dogariu, “Wide-field interferometric measurement of a nonstationary complex coherence function,” *Opt. Lett.* 42(23), 4929–4932 (2017).
- 136 A. W. van der Vaart, *Asymptotic Statistics* (Cambridge University Press, 2000).
- 137 D. W. Mackowski and M. I. Mishchenko, “Calculation of the T matrix and the scattering matrix for ensembles of spheres,” *JOSA A* 13, 2266–2278 (1996).

- 138 A. Egel, L. Pattelli, G. Mazzamuto, D. S. Wiersma, and U. Lemmer, “CELES: CUDA-accelerated simulation of electromagnetic scattering by large ensembles of spheres,” *J. Quant. Spectrosc. Radiat. Transfer* 199, 103–110 (2017).
- 139 B. D. Lubachevsky and F. H. Stillinger, “Geometric properties of random disk packings,” *J. Stat. Phys.* 60, 561–583 (1990).
- 140 M. Skoge, A. Donev, F. H. Stillinger, and S. Torquato, “Packing hyperspheres in high-dimensional Euclidean spaces,” *Phys. Rev. E* 74, 041127 (2006).
- 141 C. Schwartz and A. Dogariu, “Backscattered polarization patterns, optical vortices, and the angular momentum of light,” *Opt. Lett.* 31, 1121–1123 (2006).
- 142 C. Schwartz and A. Dogariu, “Backscattered polarization patterns determined by conservation of angular momentum,” *JOSA A* 25, 431–436 (2008).
- 143 M. V. Berry, “Interpreting the anholonomy of coiled light,” *Nature* 326, 277–278 (1987).
- 144 A. C. Maggs and V. Rossetto, “Writhing photons and Berry phases in polarized multiple scattering,” *Phys. Rev. Lett.* 87, 253901 (2001).
- 145 J. F. Nye, *Natural Focusing and Fine Structure of Light: Caustics and Wave Dislocations* (CRC Press, 1999).
- 146 E. Jakeman, “K-distributed noise,” *J. Opt. A* 1, 784–789 (1999).
- 147 A. A. Budini, “Central limit theorem for a class of globally correlated random variables,” *Phys. Rev. E* 93, 062114 (2016).
- 148 A. M. Paniagua-Diaz, I. Starshynov, N. Fayard, A. Goetschy, R. Pierrat, R. Carminati, and J. Bertolotti, “Blind ghost imaging,” *Optica* 6, 460–464 (2019).

- 149 J. Bertolotti, E. G. Van Putten, C. Blum, A. Lagendijk, W. L. Vos, and A. P. Mosk, "Non-invasive imaging through opaque scattering layers," *Nature* 491, 232–234 (2012).
- 150 R. Horstmeyer, H. Ruan, and C. Yang, "Guidestar-assisted wavefront-shaping methods for focusing light into biological tissue," *Nat. Photonics* 9, 563–571 (2015).
- 151 M. Xu, "Electric field Monte Carlo simulation of polarized light propagation in turbid media," *Opt. Express* 12, 6530-6539 (2004).